This is a preprint, the final version is subject to change, of the American Mineralogist (MSA)
Cite as Authors (Year) Title. American Mineralogist, in press.
DOI: https://doi.org/10.2138/am-2019-6890

Revision 2

Discrete Zr and REE mineralization of the Baerzhe rare-metal deposit, China

Kunfeng Qiu[1,2], Haocheng Yu[1], Mingqian Wu[1,3*], Jianzhen Geng[1,4], Xiangkun Ge[5], Zongyang Gou[1], Ryan D. Taylor[6*]

[1] State Key Laboratory of Geological Processes and Mineral Resources, School of Earth Sciences and Resources, China University of Geosciences, Beijing 100083, China

[2] Department of Geology and Geological Engineering, Colorado School of Mines, Golden, Colorado 80401, USA

[3] Department of Earth and Environmental Sciences, University of Windsor, Windsor, Ontario N9B 3P4, Canada

[4] Tianjin Center, China Geological Survey, Tianjin 300170, China

[5] CNNC Beijing Research Institute of Uranium Geology, Beijing 100029, China

[6] U. S. Geological Survey, Box 25046, Mail Stop 973, Denver Federal Center, Denver, Colorado 80225, USA

[*] Corresponding author:

aria.wu1900@gmail.com (mwu), rtaylor@usgs.gov (rtaylor)

Two tables, nine figures, and four supplementary tables

ABSTRACT

Although REE (lanthanides + Y) mineralization in alkaline silicate systems is commonly accompanied with Zr mineralization worldwide, our understanding of the relationship between Zr and REE mineralization is still incomplete. The Baerzhe deposit in NE China is a reservoir of REE, Nb, Zr, and Be linked to the formation of an Early Cretaceous, silica-saturated, alkaline intrusive complex. In this study, we use in situ laser ablation–inductively coupled plasma mass spectrometry (LA-ICP-MS) analyses of zircon and monazite crystals to constrain the relationship between Zr and REE mineralization at Baerzhe.

Three groups of zircon are identified and are differentiated based upon textural observations and compositional characteristics. Type Ia zircons display well-developed oscillatory zoning. Type Ib zircons are darker in cathodoluminescence images and have more irregular zoning and resorption features than Type Ia zircons. In addition, Type Ib zircons can locally occur as overgrowths on Type Ia zircons. Type II zircons contain irregular but translucent cores and rims with oscillatory zoning that are murky brown in color and occur in aggregates. Textural features and compositional data suggest that Types Ia and Ib zircon crystallized at the magmatic stage, with Type Ia being least-altered and Type Ib being strongly altered. Type II zircons, on the other hand, precipitated during the magmatic to magmatic-hydrothermal transition. Whereas the magnitude of the Eu anomaly is moderate in the barren alkaline granite, both magmatic and deuteric zircon exhibit pronounced negative anomalies. Such features are difficult to explain exclusively by feldspar fractionation and could indicate the presence of fluid induced

modification of the rocks. Monazite crystals occur mostly through replacement of zircon and sodic amphibole; monazite clusters are also present. Textural and compositional evidence suggests that monazite at Baerzhe is hydrothermal.

Types Ia and Ib magmatic zircon yield ^{207}Pb-corrected ^{206}Pb/^{238}U ages of 127.2±1.3 Ma and 125.4±0.7 Ma, respectively. Type II deuteric zircon precipitated at 124.9±0.6 Ma. The chronological data suggest that the magmatic stage of the highly evolved Baerzhe alkaline granite lasted less than two million years. Hydrothermal monazite records a REE mineralization event at 122.8±0.6 Ma, approximately 1 or 2 million years after Zr mineralization. We therefore propose a model in which parental magmas of the Baerzhe pluton underwent extensive magmatic differentiation while residual melts interacted with aqueous hydrothermal fluids. Deuteric zircon precipitated from a hydrosilicate liquid, and subsequent REE mineralization, exemplified by hydrothermal monazite, correlates with hydrothermal metasomatic alteration that postdated the hydrosilicate liquid event. Such interplay between magmatic and hydrothermal processes resulted in the formation of discrete Zr and REE mineralization at Baerzhe.

Key words:

Textural relationship; Zircon and monazite; In situ LA-ICP-MS analysis; Baerzhe REE-Nb-Zr-Be deposit

INTRODUCTION

Rare earth elements (REEs), in particular the heavy REEs (HREEs), are necessities in high-tech applications (Gysi and Williams-Jones 2013; Hou et al. 2015). China hosts about one-third of the world's known REE reserves and currently supplies >95% of the world's REE mine production (Chakhmouradian and Wall 2012; Weng et al. 2015). The price spikes of these commodities over the past several years, coupled with China's decision to strategically curtail exports have led to a surge in the exploration for REEs (Verplanck and Hitzman 2016). A wide variety of REE deposits have been discovered and mined, including carbonatites, ion-adsorption clays, placers, pegmatites, alkaline granites, and hydrothermal veins (Kynicky et al. 2012; Xie et al. 2016; Liu and Hou 2017).

Zirconium and REEs have been widely recognized to be spatially associated with peralkaline and alkaline igneous rocks worldwide, such as the Strange Lake deposit in Canada, the Khalzan Buregte deposit in Mongolia, and the Baerzhe deposit in China. Key aspects of REE mineralization have been well documented, including the nature of the ore-hosting granites (Dumańska-Słowik 2016; Wu et al. 2016), REE solubility and mobility in melts and fluids (e.g., Niu et al. 2008; Gysi and Williams-Jones 2013), geochemical behavior during hydrothermal mobilization (Censi et al. 2017; Dai et al. 2017), and genesis of Zr–Nb–REE mineralization (Yang et al. 2014; Kempe et al. 2015; Gladkochub et al. 2017). Much less understood is the spatio-temporal and genetic relationship between Zr and REE minerals in alkaline systems (e.g. Škoda and Novák 2007; Linnen et al. 2014; Petrella et al. 2014; Möller and Williams-Jones 2016; Wu et al.

2018). A recent mineralogical study on the sodic lujavrite from the Saima alkaline complex in NE China by Wu et al. (2016) suggested that Zr mineralization preceded REE mineralization, but this study lacked robust geochronological constraints. The Baerzhe REE-Nb-Zr-Be deposit, situated in Inner Mongolia (NE China) has an estimated reserve of 1.0 Mt of total REE oxides at an average grade of 0.57 wt%, 2.8 Mt of ZrO_2 at an average grade of 2.73 wt%, 300 Kt of Nb_2O_5 at an average grade of 0.24 wt%, and 48,470 t of BeO at an average grade of 0.05 wt% (Internal report of the LU'AN mining company 2011). Beryllium is extracted from hingganite ($(Y,REE,Ca)_2(\square,Fe^{2+})Be_2[SiO_4]_2(OH)_2$) as an important by-product (Wang and Zhao 1997). The deposit is hosted by the Early Cretaceous Baerzhe alkaline granite (Fig. 1). Previous research on the Baerzhe deposit has defined the petrogenesis of the ore-hosting Baerzhe alkaline granite (Jahn et al. 2001; Yuan et al. 2003), nature and evolution of ore-forming fluids (Sun et al. 2013), timing of the Baerzhe granite emplacement and zirconium mineralization (Zhang and Yuan 1988; Wang and Zhao 1997;Yang 2012; Yang et al. 2014), magmatic-hydrothermal processes controlling the enrichment of REE (Niu et al. 2008; Yang et al. 2011), and ore genesis (Yang et al. 2009; Qiu et al. 2014) by using petrogeochemistry, Sr-Nd-Pb-Hf-O isotopes, zircon U-Pb and whole-rock Rb-Sr geochronology, and microthermometry and Raman laser analysis on crystal-rich fluid and melt inclusions. The previous work provides a platform to build off and to investigate the textural and temporal relationship between Zr and REE mineralization in the Baerzhe alkaline silicate system.

Monazite is a REE-rich orthophosphate mineral that contains a broad array of light

rare earth elements (LREEs) and HREEs (including Y) (Zhu et al. 1997; Williams et al. 2007). Because it is present in a wide variety of rock types, and contains significant Th and U, with negligible common Pb relative to radiogenic Pb, monazite has been widely used for Th–U–Pb dating as a robust geochronometer in various geologic studies (Qiu and Yang 2011; Williams et al. 2011).

Zircon and monazite geochronology using laser ablation inductively coupled plasma mass spectrometry (LA-ICP-MS) is an important step toward a better understanding of the evolution of magmatic and hydrothermal ore deposits (Zhu and O'Nions 1999; Brown et al. 2002; Vielreicher et al. 2003; Spencer et al. 2016; Deng et al. 2017). Modern research focused on the geochronology of the Baerzhe rare-metal deposit is well established (Table 1); however, few published geochronological data provide convincing age constraints on Zr due to the use of zircon separates and no direct age data on monazite has been reported. The application of in situ compositional and geochronological analyses on the doubly polished thin sections carried out in this study prevent the loss of textural context and potential mixing of polygenetic age populations of zircon and monazite that may occur using methods that require mineral separation and grain mount preparation. However, it should be noted, that spot analyses yielding low U abundances and elevated common Pb contents need to be corrected for, along with possible matrix effects.

Mineralogical and geochemical analyses of monazite and zircon and in situ LA-ICP-MS U-Pb isotopic analyses on doubly polished thin sections were conducted in this study. The age differences between monazite (as a proxy for REE mineralization) and

129 zircon (as a proxy for Zr mineralization) provide insight into the magmatic-hydrothermal
130 evolution at the Baerzhe REE-Nb-Zr-Be deposit.
131

132 GEOLOGICAL SETTING AND PREVIOUS GEOCHRONOLOGY

133 The Baerzhe deposit (Inner Mongolia, China) is covered largely by Mesozoic
134 volcanic basins that developed along a NE- and NNE-trending deep-seated fault zone on
135 Permian basement (Fig. 1a). The REE-Nb-Zr-Be mineralized Baerzhe granite (125-123
136 Ma; Wang and Zhao 1997; Qiu et al. 2014; Yang et al. 2014) is exposed over
137 approximately 0.4 km^2. The granite comprises the West body and the East body and
138 intruded the Late Jurassic Baiyingaolao Formation consisting of andesite lavas and tuffs
139 (Fig. 1b). The East body with abundant albite and quartz is the main ore-bearing body in
140 the Baerzhe deposit (Niu et al. 2008).
141 The West body is circular at the surface (0.11 km^2) and widens with depth. It consists
142 of microcline (50-55%), quartz (30-35%), sodic amphibole (10-15), aegirine (2-7%),
143 oligoclase-albite (1-3%), and magnetite and hematite (1-3%). Accessory minerals include
144 synchysite, pyrochlore, ferrothorite, zircon, fluorite, calcite, chlorite, stilpnomelane,
145 astrophyllite, electrum, galena, sphalerite, smithsonite, and cerussite. The East body has a
146 NE-trending elongated shape (0.3 km^2) and is composed mainly of quartz (40-45%),
147 perthite (20-35%), microcline (10-15%) albite (10-15%), sodic amphibole (5-8%), aegirine
148 (0-3%), and hematite and ilmenite (3-5%). Disseminated zircon (2-8%) and higganite
149 (0-5%) are the dominant ore minerals hosting the rare-metal mineralization with minor to
150 trace amounts of pyrochlore, ferrothorite, synchysite, monazite, genthelvite,

Nb-Fe-bearing rutile, columbite, ilmenite, fluorite, calcite, and goethite (Bai et al. 1980; Ding et al. 1985). The East body was more intensely altered by albite, quartz, aegirine, and hematite. Five zones were recognized by drilling to 300 m depth: (1) pegmatitic granite, (2) ore-bearing, strongly albitized alkali granite; (3) partially albitized alkali granite; (4) weakly albitized alkali granite; and (5) porphyritic sodic amphibole granite (Fig. 1c; Sun et al. 2013; Yang et al. 2014). The East body is composed mainly of a mineralized, Na-metasomatized, transsolvus granite unit in the upper part, and a barren and weakly mineralized, sodic amphibole-rich, hypersolvus granite in the lower part.

The mineralized transsolvus granite in the upper part is commonly coarse grained with abundant miarolitic cavities, and composed of 45-50 vol% subhedral to euhedral K-feldspar that is 0.4 to 1 mm in size, 20-30 vol% subhedral to euhedral quartz which is 0.5 to 1 mm in size, 20-25 vol% albite, 1-5 vol% aegirine, and minor sodic amphibole and zircon. The barren hypersolvus granite in the lower section is usually fine grained and contains 50-55 vol% of microcline, 15-20 vol% quartz, 10-15 vol% sodic amphibole, 8-12 vol% albite, with minor aegirine and zircon (Fig. 2; Wang and Zhao 1997; Jahn et al. 2001; Yuan et al. 2007; Yang et al. 2013).

The REE-Nb-Zr-Be ores of the Baerzhe deposit are hosted by the Baerzhe igneous complex. These alkaline granites show a large diversity of medium to coarse grained textures (Fig. 2). They are characterized by high silica content (up to 75 wt.% SiO_2) and high alkali content (8.6-9.1 wt.% K_2O +Na_2O). The pegmatites are rich in volatiles (190-2,500 ppm F), but poor in aluminum (10-12 wt.% Al_2O_3). They contain elevated abundances of incompatible elements, including Rb, Y, Zr, Hf, Ta, Nb, Th, U, REEs

(except for Eu), and F, and low concentrations of CaO, MgO, P_2O_5, Ba, and Sr. They are highly fractionated with an average Nb/Ta value of 27, an average $LREE_N/HREE_N$ value of 1.3 (normalized from Masuda et al. 1973), and show "v-shaped" REE patterns enriched in Ce, but depleted in Eu (Wang and Zhao 1997; Jahn et al. 2001; Yang 2012).

Previously described mineralogical and geochemical features (Bai et al. 1980; Ding et al. 1985; Sun et al. 2013; Yang et al. 2014) have been interpreted as evidence for a multistage metasomatic alteration that resulted in pronounced compositional and mineralogical heterogeneity in alteration assemblages. The rare-metal mineralization, including Zr, Nb, and REEs, is contained in a series of minerals, including zircon, hingganite, ferrocolumbite, pyrochlore, monazite, and bastnäsite. Zircon is the only ore mineral for Zr, and REEs are predominantly contained in hingganite. The main host of Nb is columbite-(Fe).

Much recent research has focused on the geochronology of the intrusive rocks of the Baerzhe rare-metal deposit (Table 1). The Baerzhe alkaline granite host had been previously dated by three different methods, yielding relatively consistent results. Zhang and Yuan (1988) preliminarily reported the alkaline granite was emplaced at 127 Ma (six albite granite samples) using whole-rock Rb-Sr dating. The ~127 Ma age was accepted as the age of mineralization in the Baerzhe deposit until the early 2000s when newer data reported 125±2 Ma (six albite granite samples; Wang and Zhao 1997) and 127.2 Ma (alkaline granite, number of the analyzed samples not clear; Yuan et al. 2003) ages determined by whole-rock Rb-Sr. However, the applicability of the Rb-Sr method for determining the age of mineralization at Baerzhe was recently challenged (Yang 2012).

Since the Baerzhe alkaline granite is highly fractionated and contains as much as 1,545 ppm Rb and less than 5.387 ppm Sr, this could obscure the original relationship of Rb to common Sr at the time of crystallization and affect calculations of initial Sr (Clark and Černý 1987). Yang (2012) eventually argued that a Rb-Sr isochron age of 121.6±2.3 Ma (15 albite granite samples) represents the age of the highly evolved Baerzhe alkaline granite. Subsequently, high-precision LA-ICP-MS and SIMS U-Pb dating on zircon crystals separated from the mineralized and barren alkaline granite yield ages of the zircon crystals growth at 123.5±3.2 Ma (7 hydrothermal zircons; Yang et al. 2013), and 122.7±1.8 Ma (22 light colored zircons and 12 dark colored zircons; Qiu et al. 2014), and timing of the granite emplacement at 123.9±1.2 Ma (17 magmatic zircons; Yang et al. 2013), and 123.1±2.3 Ma (14 magmatic zircons; Yang 2012).

SAMPLE PREPARATIONS AND ANALYTICAL METHODS

Petrography

For the present study, 15 variably altered rock and ore samples were selected from surface exposures and subsurface drill cores. All rock samples were locally affected by late metasomatic alteration and display different degrees of ore mineralization (Fig. 2). Initially, 25 representative doubly polished thin sections (100 μm thick) were prepared for petrographic analysis and examined using a standard petrographic microscope to investigate textures and mineral assemblages, as well as relationships between constituent minerals. Full thin section images were created using a Canon Cool Scan 4000 at the Colorado School of Mines as a tool for mapping and locating the minerals identified

during petrographic observations that would be later analyzed by in situ geochemical techniques.

Five thin sections were studied using a JEOL JSM-5800LV scanning electron microscope (SEM) at the U.S. Geological Survey (USGS) in Denver, Colorado, to locate and identify the accessory minerals such as zircon and monazite grains as small as a few microns in size in direct textural context. The latter was combined with an energy dispersive spectrometer mineral identification.

Back-scattered electron (BSE) images of mineral grains collected by SEM at the USGS in Denver and the Development and Research Center of the China Geological Survey were used to characterize the distribution and intergrowth relationships of zircon and monazite and their associated minerals at 1-5 μm scales. The cathodoluminescence (CL) images were collected using a JXA-880 electron microprobe and image analysis software under operating conditions of 20 kV and 20 nA at the Tianjin Institute of Geology and Mineral Resources of CGS, to identify the internal structure, texture, and inclusions within zircon grains. Mineral abbreviations throughout the text, including those in the figures, are after Whitney and Evans (2010).

LA-ICP-MS Rare Earth Element Analyses of Zircon

In situ trace element concentrations and U-Pb ages of 32 analyses spots on 28 zircon grains were determined on a polished thin section of alkaline granite host using an Agilent 7900 ICP-MS coupled with a RESOlution M-155 193 nm laser-ablation system at the Isotopic Laboratory, Tianjin Center, China Geological Survey (Supplementary Table 1). Detailed operating conditions for the laser ablation system and the ICP-MS

instrument and data reduction are the same as described by Geng et al. (2017). The analyses were performed at an energy density of 6 J/cm^2 at a repetition rate of 6 Hz. A 29 μm spot was used for the analyses. Analyzed elements included the following: Si, Ca, Ti, Rb, Sr, Y, Nb, La, Ce, Pr, Nd, Sm, Eu, Gd, Tb, Dy, Ho, Er, Tm, Yb, Lu, Hf, Hg, Pb, Th, and U. Calibration was performed using the National Institute of Standards and Technology (NIST) 610 (Jochum et al. 2011) and SiO_2 for internal standardization (32.78 wt.%).

Helium was used as the carrier gas. NIST SRM610 and 91500 were used as external standards (Wiedenbeck et al. 2004) and ^{29}Si as an internal standard (Anczkiewicz et al. 2001). Each analysis included a background acquisition of 20-30 s and a data acquisition of 40-50 s. Zircon 91500 and Plesovice were both analyzed twice for every six unknown analyses.

All laser ablation spots were carefully selected to avoid mineral and melt inclusions and cracks in zircon grains. Only smooth LA-ICP-MS signals were chosen. After analysis, an integration of background and analytical signals, as well as time-drift correction and quantitative calibration for trace element analyses were calculated using the ICPMSDataCal 11.9 (Liu et al. 2010).

Electron-Probe Micro-Analysis of Monazite

The major element compositions of 25 monazite grains from the rare metal-bearing ores were determined on the doubly polished thin sections by using a JEOL JXA-8100 electron probe micro-analyzer equipped with four wavelength dispersive-type spectrometers at the Analytical Laboratory of the Beijing Research Institute of Uranium Geology, Beijing, China.

Operating conditions were a 20 kV accelerating voltage, a 10 nA beam current (measured on the Faraday cup), and a 2 μm focused electron beam size. The Al-*Kα*, Si-*Kα*, Mg-*Kα*, Y-*Lα*, and As-*Lα* were measured with TAP crystal, Ti-*Kα*, Fe-*Kα*, Mn-*Kα*, Hf-*Lα*, Ta-*Lα*, Ba-*Lα*, Ce-*Lα*, La-*Lα*, Eu-*Lα*, Yb-*Lα*, Tb-*Lα*, Lu-*Lα*, Tm-*Lα*, Nd-*Lβ*, Gd-*Lβ*, Sm-*Lβ* , Pr-*Lβ*, Dy-*Lβ*, Er-*Lβ*, and Ho-*Lβ* with LiF crystal, and Nb-*Lα*, U-*Mα*, Ca-*Kα*, Pb-*Mα*, P-*Kα*, Th-*Mα*, S-*Kα*, and Zr-*Lα* with PETJ crystal.

The calibration standards were as follows: albite for Al; zircon for Zr and Si; pyrope for Mg; yttrium Al garnet (synthetic) for Y; monazite for P, Ce, La, Pr, and Nd; metal uranium, hafnium, tantalum, ytterbium, gadolinium, samarium, dysprosium, erbium, holmium for U, Hf, Ta, Yb, Gd, Sm, Dy, Er, and Ho; bustamite for Ca and Mn; galena for Pb; hematite for Fe; ThO_2 (synthetic) for Th; benitoite for Ti; $KNbO_3$ (synthetic) for Nb; arsenopyrite for As; barite for S, EuP_5O_{14}, TbP_5O_{14}, and LuP_5O_{14}; and TmP_5O_{14} for Eu, Tb, Lu, and Tm. The ZAF routine was applied for data correction. The analytical data are given in Supplementary Table 2.

LA-ICP-MS U-Pb Dating of Zircon and Monazite

The zircon and monazite crystals were selected and marked on the doubly polished thin sections after locating them using an optical microscope and EPMA. The marked thin sections were placed in a specialized sample holder, which allowed documentation of the x-y coordinates of the selected crystals.

In situ U-Pb isotopic analyses were carried out using the LA-ICP-MS facility at the Isotopic Laboratory, Tianjin Center, China Geological Survey (Supplementary Tables 3, 4). Laser sampling was performed using a Neptune double focusing multiple-collector

ICP-MS (Thermo Fisher Ltd.) attached to a NEW WAVE 193 nm-FX ArF Excimer laser-ablation system (ESI Ltd.). The maximum mass dispersion is 17%. This machine has nine faraday cups: one fixed central channel and eight motorized Faraday cups. The secondary electron multiplier is bound with the central channel and the four ion counters are bound with the L4 Faraday cup. Detailed operating conditions of the laser ablation system and the ICP-MS instrument and data reduction are provided in Geng et al. (2017). $^{207}Pb/^{206}Pb$, $^{206}Pb/^{238}U$, $^{207}Pb/^{235}U$ and $^{208}Pb/^{232}Th$ ratios were calculated from measured isotope signal intensities. Mass bias, laser-induced mass fractionation and instrument drift were corrected using ICPMSDataCal 8.4 (Liu et al. 2010). Concordia diagrams and weighted mean U–Pb ages were processed using Isoplot version 3.75 software (Ludwig 2012). Common-Pb corrections were made using the method of Andersen (2002).

All zircon analyses were conducted with a beam diameter of 30 μm, an 8 Hz repetition rate, and energy density of 10 J/cm^2. GJ-1 was used as an external standard for U–Pb geochronology analyses (published TIMS ages of $^{206}Pb/^{238}U$=600.7±1.1 Ma, $^{207}Pb/^{235}U$=602.0±1.0 Ma, and $^{207}Pb/^{206}Pb$=607.7±4.3 Ma; Jackson et al. 2004). NIST SRM 610 glass was used as an external standard to calculate U, Th, and Pb concentrations of zircon. Every five analyses were followed by two analyses of the standard zircon GJ-1.

All monazite analyses were conducted with a beam diameter of 5 μm, a 5 Hz repetition rate, and energy density of 10 J/cm^2. Reference standard material 44069 (SIMS U–Pb age: 424.9±0.4 Ma; Aleinikoff et al. 2006) was analyzed after every five unknowns under identical conditions.

RESULTS

Textural Features

Zircon grains range in shape from euhedral to anhedral, with sizes up to 300 μm in width. Some euxenite, monazite, and bastnäsite grow in cracks within zircon grains.

Zircon crystals investigated herein are further classified into three types, as indicated below, based on their occurrence mode and relationship with minerals. Type Ia zircons are found as subhedral or euhedral crystals and generally display well-developed oscillatory zoning both in optical and CL images and yield condensed growth zones with relatively light rims expressed by CL imaging (Table 2, Fig. 3).

Type Ib zircons are intergrown with magmatic phases including quartz, K-feldspar, and sodic amphibole (Fig. 4). Such zircons appear darker in CL images, and in some cases form overgrowths on Type Ia zircons (Fig. 4e). More irregular zoning and resorption features are identified in Type Ib zircons (Table 2, Figs. 4e, f).

Type II zircons are the most abundant of the zircon populations at Baerzhe, and exhibit complicated core-mantle texture: irregular cores and well-developed oscillatory zoning at the rim (Table 2, Fig. 5). Rims are commonly murky brown, translucent 20-50 μm-thick mantles on magmatic cores with chaotic texture. These features are texturally distinct from Type Ia and Type Ib zircon in the same rock samples. In addition, they have replaced sodic amphibole. The REE-bearing minerals, including euxenite and bastnäsite also occur through replacement of Type II zircons, suggesting that these REE minerals postdated the Type Ia and Ib zircons.

As shown in Fig. 6, monazite crystals in this study are subhedral to anhedral (Table

2), and generally are interstitial as discrete grains up to 150 μm in width in the matrix in contact with margins of quartz and K-feldspar (Fig. 6b) or as small (<100 μm in width) inclusions (Fig. 6a) in primary minerals, mainly in quartz, albite, K-feldspars and sodic amphibole. Monazite shows mottled zoning in BSE images. In addition, the aggregation textures of monazite grains occurring in clusters within a restricted area and the metasomatic growth texture of monazite which replaces zircon rims testifies that the monazite in this study is younger than zircon.

Mineral Compositions of Zircon and Monazite

Representative grains of the three textural populations of zircons were analyzed on four doubly polished thin sections (#87b, #106a, #106b, and #108a). Trace element characteristics are given in Supplementary Table 1 and illustrated in Figure 7.

Type Ia zircons have concentrations of REE = 0.90-1.15%, and Th = 346-573 ppm. Their total Pb contents range from 101 to 595 ppm, and $(Lu/Yb)_{CN}$ =1.08-2.01. They yield LREE/HREE ratios from 0.01 to 0.03 and have distinct negative Eu anomalies (Eu/Eu*=0.01~0.03, where $Eu^* = \sqrt{(Sm)_N \times (Gd)_N}$) (Fig. 7a). This type of zircon is characterized by a flat and low LREE pattern, and a strongly enriched HREE pattern (Supplementary Table 1, Fig. 7a).

Type Ib zircons have REE concentrations of 0.03-0.36%, and Th concentrations of 60-1,668 ppm. They have total Pb contents of 83 to 196 ppm, and $(Lu/Yb)_{CN}$ ratios ranging from 0.63 to 0.83. A broad range of LREE concentrations among samples is observed in Fig. 7b, which clearly illustrates the overlap in their chondrite-normalized

354 REE trends. A moderate enrichment of LREE relative to HREE (Gd to Er) with
355 LREE/HREE=0.17-5.03 was determined, as well as a pronounced negative Eu anomaly
356 (Eu/Eu∗=0.01-0.06) in the chondrite-normalized REE patterns. The Ce anomalies
357 (Ce/Ce* ratios, where $Ce^{*} = \sqrt{(La)_N \times (Pr)_N}$) varying from 0.24 to 2.10 was observed in
358 some cases (Fig. 7b). Most Type Ib zircons are enriched and show negative slope patterns
359 in LREE (Supplementary Table1, Fig. 7b), and commonly show moderately enriched
360 HREE patterns (Supplementary Table 1, Fig. 7b).

361 Type II zircons have REE concentrations of 0.57-1.76 %, and Th concentrations of
362 295-2,190 ppm. They have total Pb contents of 51 to 162 ppm, and $(Lu/Yb)_{CN}$=0.46-0.73,
363 and are markedly LREE enriched with LREE/HREE=0.04-2.96, thus exhibiting flat
364 chondrite-normalized REE patterns (Supplementary Table 1). Type II zircons have
365 notable negative Eu anomalies (Eu/Eu∗=0.02-0.03), weak negative Ce anomalies
366 (Ce/Ce∗=0.94-1.26) (Fig. 7c).

367 Twenty-five spots on twenty-two monazite grains were analyzed for trace element
368 composition (Supplementary Table 2). They have 0.15 to 1.74 wt. % SiO_2 and 28.34 to
369 30.59 wt. % P_2O_5, and ThO_2 abundances ranging from 0.26 to 4.25 wt.%. Their LREE
370 concentrations range from 53.09 to 59.17 wt. % and total REE concentrations from 54.08
371 to 59.57 wt.%. LREE/HREE ratios range from 49.22 to 312.07, and are typified by
372 significant enrichment of chondrite-normalized LREE over HREE with a very steep
373 negative slope. A weak positive Ce anomaly with Ce/Ce∗ ranges from 1.05 to 1.29. The
374 monazite grains are typified by a distinct positive Eu anomaly display with Eu/Eu∗
375 ranging from 1.13 to 22.34 (Fig. 7d).

376

377 **Geochronology of Zircon and Monazite**

378 In situ LA-ICP-MS U-Pb data collected on zircon and monazite grains of doubly
379 polished thin sections are summarized in Supplementary Tables 3 and 4, and subsets of
380 the isotopic ages are illustrated on the Tera–Wasserburg Concordia diagram in Fig. 8.
381 The age of the Type Ia zircons was determined by 13 analyses from 9 zircon crystals from
382 sample #87b and #106a, and yielded 69-3,161 ppm U, 6-734 ppm Th, with Th/U ratios
383 of 0.03 to 1.30. The ^{207}Pb-corrected ^{206}Pb/^{238}U ages range from 122.8±1.5 Ma to
384 132.8±1.4 Ma and give a lower intercept age of 127.2 ± 1.3 Ma (MSWD=1.7, n =13).
385 The age of the Type Ib zircons was determined by 28 analyses from 15 crystals from
386 sample #108a, and yielded 673-4,886 ppm U, 84-2,933 ppm Th, with Th/U ratios of 0.06
387 to 1.46. They have ^{207}Pb-corrected ^{206}Pb/^{238}U ages ranging from 122.8±1.5 Ma to
388 132.8±1.4 Ma, with a lower intercept age of 125.4±0.7 Ma (MSWD=0.72, n =28).
389 The age of Type II zircons was determined by 29 analyses of 20 crystals from
390 sample #106b and #108a, and yielded 1,124-5,137 ppm U, 304-3,131 ppm Th, with
391 Th/U ratios of 0.09 to 1.44. All of these data are concordant and have ^{207}Pb-corrected
392 ^{206}Pb/^{238}U ages ranging from 122.8±1.5 Ma to 132.8±1.4 Ma that produce a lower
393 intercept age of 124.9±0.6 Ma (MSWD=1.1, n =29).
394 The age of monazite was determined by 37 analyses on 22 monazite crystals from
395 sample #106b and #108a. Analyses on monazite crystals have U concentrations of
396 49-1,884, and Th concentrations of 11,900-88,139 ppm with Th/U ratios from 42.46 to
397 437.79. They yield ^{207}Pb-corrected ^{206}Pb/^{238}U ages ranging from 122.9±4.8 Ma to

137.3±2.0 Ma, consistent with a lower intercept age at 122.8±0.6 Ma (MSWD = 0.95, n =37).

DISCUSSION

Origins of Zircon and Monazite

Distinguishing with certainty between hydrothermal, deuteric, and magmatic zircon and monazite was greatly aided by studying their texture, occurrence, and their associated mineral assemblages. The REE distribution patterns have also been successfully applied as a sensitive indicator to determine the formation conditions of magmatic and metasomatic rocks (Yang et al. 2014; Taylor et al. 2015). Textural and compositional evidence, acquired during this study, divide zircons into three types.

Individual type Ia and Ib zircons are interpreted to be magmatic in origin due to their generally well-developed oscillatory growth zoning (Figs. 3, 4) and their REE patterns that are typical of magmatic zircon (Fig. 7a, b). Compared to primary magmatic zircon, Type Ia zircons are slightly enriched in LREE, and Type Ib zircons are strongly enriched in LREE and depleted in HREE. Such observations suggest that these magmatic zircons suffered variable degrees of alteration, with Type Ia being least-altered and Type Ib being strongly altered. The alteration results in altered grains displaying irregular zoning with resorption features cross-cutting the primary zoning, and/or metasomatic overgrowths on primary or less-altered zircon crystals (Figs. 3d, 4e). Such irregular zoning and resorption features are similar to textures that were produced in relation to magma mixing processes reported by Tepper and Kuehner (1999).

The textural and geochemical differences found with Type II zircons suggest that they are not typical magmatic phases such as Types Ia and Ib. They display complicated core-mantle textures and have been identified along the cleavage of sodic amphibole, which is a typical magmatic phase associated with K-feldspar, quartz, and magmatic zircons (Fig. 5). Such paragenetically later textural features indicate that the Type II zircon belong to a younger generation than Types Ia and Ib.

Type II zircon shows significant enrichment of REE (Supplementary Table 1, Table 2) compared to both the least and strongly altered magmatic zircons and alkaline granite whole-rock samples (at least two orders of magnitude). Non-formula elements U, Hf, Nb, Ta, Ti, and LREE concentrations are enriched relative to magmatic zircon in the same rock also suggest that the Type II zircons are crystalized from highly fractionated fluids (Supplementary Table 1, Table 2). Metal behavior varies between different media and results in crystals with chemical characteristics dependent upon what they crystallized from. Deuteric crystals, such as Type II zircons, can form from a hydrosilicate liquid produced during the magmatic to hydrothermal transition from a media with transitional properties between a melt and a fluid. This is consistent with larger-radii LREE being incompatible in the magmatic zircon structure (Hanchar and Westrenen 2007) and more compatible in magmatic fluids (Bakker and Elburg 2006).

No pristine igneous zircon is observed, whose REE pattern may be dominated by the lattice strain model and characterized by a steep positive slope, low La (≤0.1 ppm), positive Ce, and negative Eu anomalies (Hoskin 2005), which is the consequence of the exclusion of the large ionic radii LREEs from the crystal structure during crystallization

(Hanchar and van Westrenen 2007). A majority of zircon grains examined in our study were LREE enriched, thus exhibiting relatively flat patterns on chondrite-normalized diagrams. Comparable variability in chondrite-normalized REE patterns has also been observed in several other studies (e.g., Hoskin 2005; Marsh and Stockli 2015; Skipton et al. 2016; Kelly et al. 2017), and the mechanisms that may form LREE-enriched parent zircon remain enigmatic (Chapman et al. 2016), but could include a LREE-enriched source melt (Hoskin et al. 2000), complex substitutions (Hoskin and Schaltegger 2003), and sampling of micro-inclusions during analysis (Hanchar and van Westrenen 2007). Any combination of these possibilities may be responsible for the growth of zircon that deviates from the expected REE pattern (cf. Marsh and Stockli 2015). While the magnitude of the Eu anomaly is moderate in barren alkaline granite whole-rock samples (Eu/Eu*=0.05-0.65), both magmatic (Eu/Eu*=0.01-0.06) and deuteric zircons (Eu/Eu*=0.02-0.03) exhibit more pronounced negative anomalies. Such pronounced Eu anomalies are difficult to explain exclusively by feldspar fractionation and could indicate the importance of late fluid activity.

The hydrothermal monazite at Baerzhe may be distinguished from igneous monazite by its unique geochemical signature, its occurrence, and its common association with hydrothermal mineral assemblages. Monazite crystals occur in clusters within a restricted area showing distinct petrographic characteristics of hydrothermal monazite (Fig. 6) (Schandl and Gorton, 2004). REE-bearing minerals including euxenite and bastnäsite also occur in the cracks of deuteric Type II zircons (Figs. 5d-e) suggesting that the REE mineralization postdated the late magmatic processes. Monazite commonly grows along

464 the cleavage of sodic amphibole and metasomatizes zircon, suggesting that they are
465 hydrothermal in origin.

466 Igneous and hydrothermal monazite grains commonly have similar morphologies
467 making geochemical evidence discriminating between hydrothermal and igneous
468 monazite critical to their identification (Wall and Mariano 1996; Schandl and Gorton,
469 2004; Taylor et al. 2015). First, the monazite at Baerzhe has lower ThO_2 abundance (2
470 wt. % on the average) distinct from that of magmatic monazite (typically >5 wt. %;
471 Schandl and Gorton, 2004). Second, hydrothermal monazite patterns show a very steep
472 negative trend revealing a distinct fractionation between LREE and HREE. Third,
473 hydrothermal monazite is enriched in Eu (Fig. 7d), notably distinguishing it from igneous
474 monazite which crystallizes in equilibrium with plagioclase and therefore has a
475 pronounced negative Eu anomaly (Zhu and O'Nions 1999). This is because unlike
476 magmatic plagioclase that preferentially incorporates Eu, non-magmatic/hydrothermal
477 systems typically evolve in the absence of plagioclase (Kim et al. 2005). The overall REE
478 abundances are broadly similar but can be locally different, because the REE
479 geochemistry of hydrothermal (or metamorphic) monazite can be subtly influenced by
480 the REE contributions of the local country rock or the source from a number of different
481 geological settings (Zhu et al. 1997; Kositcin et al. 2003).

482 Geochemically, the REE distribution patterns of hydrothermal monazite grains
483 reveal distinct fractionation between LREE and HREE, and a pronounced positive Eu
484 anomaly. This indicates that the crystallization of monazite is distinct from zircon, which
485 is affected by feldspar in the melt (Fig. 7d). These petrologic, mineralogical, and

compositional traits suggest that the monazite at Baerzhe is hydrothermal in origin.

Timing of Zr and REE Formation

In situ LA-ICP-MS U-Pb analyses of zircon and monazite bracket the magmatic, late magmatic (deuteric) and hydrothermal stages into a geochronological context that is consistent with their textural relationship, unlike age determinations of previous studies. The Type Ia and Type Ib magmatic zircons yield the ^{207}Pb-corrected ^{206}Pb/^{238}U ages at 127.2±1.3 Ma and 125.4±0.7 Ma (Figs. 8a-b), respectively. The Type II deuteric zircons crystallized at 124.9±0.6 Ma (Fig. 8c). Our data suggest that magmatic crystallization and late magmatic processes of the highly evolved Baerzhe alkaline granite lasted less than ~2 million years as shown by the combined Rb-Sr ages at ca. 125.7-125.0 Ma of the Baerzhe alkaline granite whole-rock samples (Zhang and Yuan 1988; Wang and Zhao 1997; Yuan et al. 2003; Yang 2012), and zircon U-Pb ages ranging from 126 Ma to 123 Ma (Yang 2012; Qiu et al. 2014; Yang et al. 2014) reported in the literature. The hydrothermal monazite records a REE mineralization event at 122.8±0.6 Ma, which is possibly 1 or 2 million years later, but coeval within reported errors. This is consistent with the textural relationship that the REE mineralization at Baerzhe is slightly later than the Zr mineralization (Table 2, Fig. 9).

Implications on Links Between Zr and REE Mineralization at Baerzhe

Several different mechanisms responsible for the formation of Zr–Nb–REE mineralization have been presented. Gysi and Williams-Jones (2013) proposed that saline

HCl–HF-bearing fluids created pathways during acidic alteration from the pegmatite cores outward, leading to the mobilization of REE and Zr due to progressive alteration of primary silicate minerals and increased acidity upon cooling. Kempe et al. (2015) proposed a preliminary multistage metasomatic genetic model assuming that a silica- and carbonate-rich fluid system was responsible for the early alteration, that yielded extreme concentrations of Zr, Nb, and LREE, and occurred late during or postdating the intrusion/extrusion of the silica-saturated magmas. A "Li-F granite-type" fluid system was active during the late alteration resulting in enrichment of Y and HREE. The interplay of all these processes resulted in the formation of complex, economic Zr–Nb–REE mineralization at Khalzan Buregte (Western Mongolia). Wu et al. (2016) recognized that both Zr and REE were strongly incompatible in the sodic melt, but that Zr mineralization preceded REE mineralization in the Triassic Saima alkaline complex (Liaodong Peninsula, NE China). The main Zr-REE mineralization in the Saima lujavrite resulted from the high peralkalinity, (Na+K)/Al molar ratio (1.2) and HFSE contents (1.4 wt.%), low oxygen fugacity (ΔFMQ =−0.5 to −2.0), and the intensive activity of water and volatiles of its evolving magma. Gladkochub et al. (2017) argued a magmatic origin of the Katugin Ta-Nb-Y-Zr (REE) deposit (southern Siberia, Russia) rather than the previously proposed metasomatic fault-related origin, and most of the ore minerals crystallized from the silicate melt during the magmatic stage. Mikhailova et al. (2017) studied the Zr- and REE-bearing Western Keivy peralkaline granite massif (Kola Peninsula, NW Russia), and discovered that the behavior of REE and Zr was controlled by alkalinity of melt/solution, which, in turn, was controlled by crystallization of

alkaline pyroxenes and amphiboles at a late magmatic stage. Crystallization of mafic minerals leads to a sharp increase of K_2O contents and decrease of SiO_2 contents that in turn cause a decrease of melt viscosity and REE and Zr solubility in the liquid. Therefore, REE and Zr immediately precipitated as zircon and REE-minerals. Dai et al. (2018) studied the Nb–Zr–REE–Ga enrichment in Lopingian altered alkaline volcanic ashes (Yunnan, China), and argued that the ore-forming process represents a combination of alkaline magmatism, hydrothermal alteration, explosive volcanism, and lateritic weathering associated with later influx of meteoric and, in some cases, marine waters under lower-temperature conditions (Deng et al., 2014). These were not separate processes, but were contemporaneous, and are specifically related to volcanically active continental regions within humid climates.

Geochronology, major and trace element geochemistry, and isotope data from previous studies suggest that the Early Cretaceous alkaline granite was derived by melting of a dominantly juvenile mantle component with subordinate recycled ancient crust and is genetically responsible for the Baerzhe REE-Nb-Zr-Be deposit. Niu et al. (2008) conducted Raman spectroscopy and microthermometry on crystal-rich fluid inclusions in quartz of the ore-bearing alkaline granite, and recognized that the trapped minerals in the inclusions are predominantly silicate minerals including feldspar and mica, as well as minor REE minerals. They therefore proposed that the genesis of the ore-bearing alkaline granite was directly related to the magmatic-hydrothermal transition process, and the wide distribution of the REE minerals in the crystal-rich fluid inclusions indicates the REE had already been enriched sufficiently in the alkaline granite during the

552 magmatic-hydrothermal stage of magma evolution, and the REE mineralization was
553 constrained by the fluid derived from this stage. Yang et al. (2013) reported that
554 hydrothermal zircon yields extremely negative $\delta^{18}O$ values of -18.12 ‰ to -13.19 ‰,
555 which are distinguished from magmatic zircon (2.79~5.10 ‰) with numbers close to
556 mantle values (5.3±0.3 ‰; Valley et al. 1998). Such a great shift of O isotopes from
557 magmatic to hydrothermal zircon with consistent Hf composition at Baerzhe indicates a
558 physicochemical change of the ore-forming environment.

559 Textural relations and compositional variation among the characteristic
560 Zr-REE-bearing minerals record that Zr mineralization preceded REE mineralization at
561 Baerzhe. Geochronological results collected by in situ LA-ICP-MS U-Pb dating are
562 consistent with texturally determined paragenetic sequences of Zr-REE-bearing minerals,
563 and demonstrate that the Zr and REE mineralization at Baerzhe is associated with
564 distinct magmatic, transitional, and hydrothermal events. The first two events were
565 responsible for the Zr mineralization that occurred late during or postdating the
566 intrusion/extrusion of the silica-saturated magmas. The parental magmas for the Baerzhe
567 granites underwent extensive magmatic differentiation, during which intense interaction
568 of the residual melts with aqueous hydrothermal fluids (probably rich in F and Cl)
569 resulted in the non-charge-and-radius-controlled trace element behavior. This is recorded
570 by the characteristic composition and chronology of the magmatic and deuteric zircons.
571 The age of deuteric zircon is indistinguishable from magmatic zircon, indicating
572 precipitation from a fluid evolved from the magma during the final stages of
573 crystallization. The youngest event resulted in REE mineralization at 122.8±0.6 Ma, less

574 than 2 million years after Zr mineralization. The interplay of all these processes resulted
575 in the formation of complex REE-Nb-Zr-Be mineralization at Baerzhe.

576 The magmatic through deuteric origins of Zr mineralization and hydrothermal
577 origin of REE mineralization have been recorded by the geochemical signatures in
578 addition to observations of metasomatic replacement of zircon by monazite. The
579 Baerzhe granites show the characteristic trace element patterns of rare-metal granites, but
580 the magmatic and deuteric zircons yield absolute abundances of REE that differ by as
581 much as two orders of magnitude. One possible explanation of their REE patterns is a
582 late magmatic exsolution of volatiles from the granitic melt. This implies the existence of
583 originally fluid-rich magmas in the alkaline series. The compositions of zircons were
584 significantly altered by these subsequent hydrothermal fluids. Their "enriched-type" REE
585 distribution patterns are similar to those present in some of the Gurvan Uneet and Ulaan
586 Uneet zircon samples (Kempe et al. 2015), which have elevated Zr, Nb, and LREE
587 contents as well as LREE/HREE fractionation that is inferred to be caused by an
588 external fluid.

589 The magmatic and deuteric zircons as well as mineralized granite have pronounced
590 negative Eu anomalies compared to that of barren granite (Fig. 7), which yield REE
591 distribution patterns characteristic of evolved magmatic rocks. Such pronounced Eu
592 anomalies are difficult to explain exclusively by feldspar fractionation and could indicate
593 the importance of fluid activity affecting their compositional characteristics. This
594 assumption is also strengthened by the appearance of positive Eu anomalies documented
595 in hydrothermal monazite.

Two of the zircon populations studied are LREE enriched, and the deuteric zircons are more enriched in LREE than the magmatic zircons. In addition, the strongly altered Type Ib magmatic zircons are more enriched in LREE than the least-altered Type Ia magmatic zircons, and both the least and strongly altered magmatic zircons are enriched in HREE but with similar LREE compared to that of the barren and mineralized alkaline granite. This suggests that effects of the hydrothermal metasomatism during later REE mineralization stage to the REE budget of both magmatic and deuteric zircons is significant. We infer that their distinct features and the LREE enrichment are an indication of the activity of LREE-rich fluids occurring shortly after plutonic emplacement and crystallization. This corresponds to the fairly heterogeneous Th/U values throughout the zircons (Supplementary Table 3), which have likely been modified by hydrothermal fluids.

Previous studies had difficulty in explaining the origin of Type II zircons at Baerzhe. Yang et al. (2013, 2014) proposed that the abundant non-magmatic zircons, which are characterized by tetragonal dipyramidal morphology, murky and featureless textures, LREE-enrichment, and high common-lead compositions, are hydrothermal. However, the fact that the Type II zircons are generally found interstitial to albite, K-feldspars, quartz, and sodic amphibole and no Type II zircon has been observed among the hydrothermal veins most likely suggests that they are not hydrothermal (*sensu stricto*). In addition, although the solubility of Zr in hydrothermal systems has not been measured directly (Linnen et al. 2014), it could only reach several hundred parts per billion (ppb) in hydrothermal fluids, based on published thermodynamic data (Migdisov et al. 2011).

Such low solubility is therefore difficult to transport significant concentrations of Zr in typical hydrothermal aqueous fluids. Hydrosilicate liquids (HSL) can transport high field strength elements in great abundance (Smirnov et al. 2017). At present, the HSL were found not only in experiments but also in "melt/fluid" inclusions entrapped in quartz and other minerals within miarolitic cavities in granite pegmatites and rare-metal granites (Thomas and Davidson, 2016). The HSL routinely form in the magmatic-hydrothermal transition, and have transitional properties between an aqueous fluid and a melt (Smirnov et al. 2012). Experimental investigations showed that the HSL are very effective in extracting, concentrating, and transporting rare metals and should be considered as potentially important media of ore metal transport and mineral formation at the stage of transition from magmatic to hydrothermal crystallization in granitic and pegmatitic systems (Smirnov et al. 2006, 2017). The compositional characteristics and textural observations of Type II zircons at Baerzhe are consistent with a deuteric origin likely precipitated from a hydrosilicate liquid.

IMPLICATIONS

Direct geochronological constraints on Zr and REE mineralization conducted on the Baerzhe REE-Nb-Zr-Be deposit are reported herein. Using in situ LA-ICP-MS U-Pb dating on zircon and monazite grains eliminates the loss of textural context and potential mixing of polygenetic zircon and monazite age populations, successfully determining discrete Zr and REE crystallization events.

Textural and geochemical characterizations distinguished the least-altered magmatic

zircon (Type Ia), the strongly altered magmatic zircon (Type Ib), and deuteric/late magmatic zircon (Type II). The crystallization of magmatic zircon, altered zircon, deuteric zircon, and monazite occurred at 127.2±1.3 Ma, 125.4±0.7 Ma, 124.9±0.6 Ma, and 122.8±0.6 Ma, respectively. Subtle age gaps bracket a ca. 2 million year magmatic-deuteric event of the highly fractionated Baerzhe alkaline granite, and document a magmatic-deuteric process for Zr mineralization, followed by a subsequent hydrothermal REE-precipitating event.

The parental magmas of Baerzhe have undergone extensive magmatic differentiation, during which the residual melts interacted with aqueous hydrothermal fluid. The deuteric zircon is interpreted to have precipitated from a hydrosilicate liquid (HSL), based on the chemical and textural characteristics observed in this study. The subsequent REE mineralization is likely related to the metasomatic alteration from external fluid sources. The interplay of these processes resulted in the formation of a complex, economic REE-Nb-Zr-Be deposit at Baerzhe.

These observations provide distinctions between specific events linked to Zr and REE mineralization. Ascertaining whether or not the Zr and REE mineralization share the same source and evaluating their ore-forming conditions are critical for exploration. A better understanding of the genetic model for rare-metal deposits requires more work on hydrothermal fluids and P-V-T-X conditions of melt and fluid inclusions, oxygen isotopes of zircon, monazite, feldspar, and quartz.

ACKNOWLEDGEMENTS

We are indebted to Jun Deng, Jade Star Lackey, Emily Peterman, and Michael Williams for thoughtful discussions concerning zircon and monazite morphology and geochemistry. Heather Lowers and Mike Pribil at the U.S. Geological Survey provided instruction, advice, and assistance during SEM and EPMA data collection. Critical and thorough reviews by Callum Hetherington, Charles Thorman, Graham Lederer, and an anonymous reviewer greatly improved the quality of the manuscript. This research was financially supported by the National Basic Research Program of China (2015CB452606), the National Natural Science Foundation of China (41702069, 41773030), the Fundamental Research Funds for the Central Universities China (2652018125, 2652018141), Open Research Project from the State Key Laboratory of Geological Processes and Mineral Resources at the China University of Geosciences (GPMR201812), and the 111 Project of the Ministry of Education of China (B07011). K-F Qiu gratefully acknowledges the support of the China Scholarship Council, Society of Economic Geologists, China Postdoctoral Foundation, and K.C.WONG Education Foundation, Hong Kong. Any use of trade, product, or firm names is for descriptive purposes only and does not imply endorsement by the U.S. government.

REFERENCES CITED

Aleinikoff, J.N., Schenck, W.S., Plank, M.O., Srogi, L., Fanning, C.M., Kamo, S.L. and Bosbyshell, H. (2006) Deciphering igneous and metamorphic events in high-grade rocks of the Wilmington complex, Delaware: morphology, cathodoluminescence

683 and backscattered electron zoning, and shrimp U-Pb geochronology of zircon and
684 monazite. Geological Society of America Bulletin, 118, 39-64.
685 Anczkiewicz, R., Oberli, F., Burg, J.P., Villa, I.M., Gunther, D. and Meier, M. (2001)
686 Timing of normal faulting along the Indus suture in Pakistan Himalaya and a case of
687 major $^{231}Pa/^{235}U$ initial disequilibrium in zircon. Earth and Planetary Science Letters,
688 191, 101-114.
689 Andersen, T. (2002) Correction of common lead in U–Pb analyses that do not report
690 ^{204}Pb. Chemical Geology, 192, 59-79.
691 Ba Bai, G., Yuan, Z.X., Ding, X.S. and Sun, L.R. (1980) Discussion on the petrogenesis
692 and minerogenesis of the rare-metal bearing alkaline granites in Baerzhe Jilin
693 Province. Chinese Academy of Geological Sciences Bulletin of the Institute of
694 Mineral Deposits, 1, 97-113 (in Chinese with English abstract).
695 Bakker, R.J. and Elburg, M.A. (2006) A magmatic-hydrothermal transition in Arkaroola
696 (northern Flinders Ranges, south Australia): From diopside–titanite pegmatites to
697 hematite–quartz growth. Contributions to Mineralogy and Petrology, 152, 541-569.
698 Brown, S.M., Fletcher, I.R., Stein, H.J., Snee, L.W. and Grooves, D.I. (2002)
699 Geochronological constraints on pre–, post–mineralization events at the world–class
700 Cleo gold deposit, Eastern Goldfields Province, Western Australia. Economic
701 Geology, 97, 541-559.
702 Censi, P., Inguaggiato, C., Chiavetta, S., Schembri, C., Sposito, F., Censi, V. and Zuddas,
703 P. (2017) The behaviour of zirconium, hafnium and rare earth elements during the
704 crystallisation of halite and other salt minerals. Chemical Geology, in press, DOI:
705 10.1016/j.chemgeo.2017.02.003.
706 Chakhmouradian, A.R., and Wall, F. (2012) Rare earth elements: Minerals, mines,
707 magnets (and more). Elements, 8, 333-340.

Chapman, J.B., Gehrels, G.E., Ducea, M.N.,Giesler, N., and Pullen, A. (2016) A new method for estimating parent rock trace element concentrations from zircon. Chemical Geology, 439, 59-70.

Clark, G.S., and Černý, P. (1987) Radiogenic ^{87}Sr, its mobility, and the interpretation of Rb-Sr fractionation trends in rare-element granitic pegmatites. Geochimica et Cosmochimica Acta, 51, 1011-1018.

Dai, S.F., Nechaev, V.P., Chekryzhov,I.Y., Zhao, L.X., Vysotskiy, S.V., Graham, I., Ward, C.R., Ignatiev, A.V., Velivetskaya, T.A., Zhao, L., French, D., and Hower, J.C. (2018) A model for Nb–Zr–REE–Ga enrichment in Lopingian altered alkaline volcanic ashes: Key evidence of H-O isotopes. Lithos, 302-303, 359-369.

Dai, S.F., Ward, C.R., Graham, I.T., French, D., Hower, J.C., Zhao, L., and Wang, X. (2017) Altered volcanic ashes in coal and coal-bearing sequences: A review of their nature and significance. Earth Science Reviews, 175, 44-74.

Deng, J., Wang, Q.F., Li, G.J., and Santosh, M. (2014) Cenozoic tectono-magmatic and metallogenic processes in the Sanjiang region, southwestern China. Earth–Science Reviews, 138(11), 268-299.

Deng, J., Wang, Q.F., and Li, G.J. (2017) Tectonic evolution, superimposed orogeny, and composite metallogenic system in China. Gondwana Research 50, 216-266.

Ding, X.S., Bai, G. and Yuan, Z.X. (1985) A study of mineralogical characteristics of some rare-metal alkaline granites in Inner Mongol Autonomous Region. Bulletin of the Institute of Mineral Deposits, Chinese Academy of Geological Sciences, 2, 97-113 (in Chinese with English abstract).

Dostal, J. (2016) Rare metal deposits associated with alkaline/peralkaline igneous rocks. Rev. Economic Geology, 18, 33-54.

Dumańska-Słowik, M. (2016) Evolution of mariupolite (nepheline syenite) in the alkaline Oktiabrski Massif (Ukraine) as the host of potential Nb–Zr–REE mineralization. Ore Geology Reviews, 78, 1-13.

Feng, S.Z. (2000) Geological characteristic and ore genesis of rare metal and rare-earth ore deposit in Baerze alkalic granite, Inner Mongolia. Volcanology and Mineral Resources, 21, 137-149 (in Chinese with English abstract).

Geng, J.Z., Qiu, K.F., Gou, Z.Y., and Yu, H.C. (2017) Tectonic regime switchover of Triassic Western Qinling Orogen: Constraints from LA-ICP-MS zircon U–Pb geochronology and Lu–Hf isotope of Dangchuan intrusive complex in Gansu, China. Chemie der Erde-Geochemistry, 77, 673-651.

Gladkocub, D.P., Donskaya, T.V.,and Sklyarov, E.V. (2017) The unique Katugin rare-metal deposit (southern Siberia): Constraints on age and genesis. Ore Geology Reviews, 91, 246-263.

Gysi, A.P., and Williams-Jones, A.E. (2013) Hydrothermal mobilization of pegmatite-hosted REE and Zr at Strange Lake, Canada: A reaction path model. Geochimica et Cosmochimica Acta, 122, 324-352.

Hanchar, J.M., and Westrenen, W.V. (2007) Rare earth element behavior in zircon-melt systems. Elements, 3, 37-42.

Hoskin, P.W.O. (2005) Trace-element composition of hydrothermal zircon and the alteration of hadean zircon from the Jack Hills, Australia. Geochimica et Cosmochimica Acta, 69, 637-648.

Hoskin, P.W.O., and Ireland, T.R. (2000) Rare earth element chemistry of zircon and its use as a provenance indicator. Geology, 28, 627.

Hoskin, P.W.O., and Schaltegger, U. (2003) The composition of zircon and igneous and metamorphic petrogenesis. Reviews in Mineralogy and Geochemistry, 53, 27-62.

Hou, Z.Q., Liu, Y., Tian, S.H., Yang, Z.M., and Xie, Y.L. (2015) Formation of carbonatite-related giant rare-earth-element deposits by the recycling of marine sediments. Scientific Reports, 5, 10231.

Jackson, S.E., Pearson, N.J., Griffin, W.L., and Belousova, E.A. (2004) The application of laser ablation-inductively coupled plasma-mass spectrometry to in situ U-Pb zircon geochronology. Chemical Geology, 211, 47-69.

Jahn, B.M. (2004) The Central Asian Orogenic Belt and growth of the continental crust in the Phanerozoic. InJ. Malpas C.J.N. Fletcher, J.C. Aitchison, Eds., Aspects of the Tectonic Evolution of China. Geological Society London Special Publications 226, 73-100.

Jahn, B.M., Wu, F.Y., Capdevila, R., Martineau, F., Zhao, Z.H., and Wang, Y.X. (2001) Highly evolved juvenile granites with tetrad REE patterns: the Woduhe and Baerzhe granites from the Great Xing'an Mountains in NE China. Lithos, 59, 171-198.

Jochum, K.P., Weis, U., Stoll, B., Kuzmin, D., Yang, Q., Raczek, I., Jacob, D.E., Stracke, A., Birbaum, K., Frick, D.A., Günther, D., and Enzweiler, J. (2011) Determination of reference values for NIST SRM 610–617 glasses following ISO guidelines. Geostandards and Geoanalytical Research, 35, 397-429.

Kelly, C.J., Schneider, D.A., Jackson, S.E., Kalbfleisch, T., and McFarlane, C.R. (2017) Insights into low- to moderate-temperature recrystallization of zircon: Unpolished crystal depth profile techniques and geochemical mapping. Chemical Geology, 449, 82-98.

Kempe, U., Möckel,R., Graupner, T., Kynicky, J., and Dombond, E. (2015) The genesis of Zr–Nb–REE mineralisation at Khalzan Buregte (Western Mongolia) reconsidered. Ore Geology Reviews, 64, 602-625.

781 Kositcin, N., McNaughton, N.J., Griffin, B.J., Fletcher, I.R., Groves, D.I., and
782 Rasmussen, B. (2003) Textural and geochemical discrimination between xenotime
783 of different origin in the Archaean Witwatersrand Basin, South Africa. Geochimica
784 et Cosmochimica Acta, 67, 709-731.
785 Kynicky, J., Smith, M.P., and Xu, C. (2012) Diversity of rare earth deposits: The key
786 example of China. Elements, 8, 361-367.
787 Linnen, R.L., Samson, I.M., Williams-Jones, A.E., and Chakhmouradian, A.R. (2014)
788 Geochemistry of the Rare-Earth Element, Nb, Ta, Hf, and Zr Deposits. In D.H.
789 Heinrich and K.K. Turekian Eds., Treatise on Geochemistry. Pergamon, Oxford.
790 Second Edition, 13. 543-568.
791 Liu, Y., and Hou, Z.Q. (2017) A synthesis of mineralization styles with an integrated
792 genetic model of carbonatite-syenite-hosted REE deposits in the Cenozoic
793 Mianning-Dechang REE metallogenic belt, the eastern Tibetan Plateau,
794 southwestern China. Journal of Asian Earth Sciences, 137, 35-79.
795 Liu, Y.S., Hu, Z.C., Zong, K.Q., Gao, C.G., Gao, S., Xu, J., and Chen, H.H. (2010)
796 Reappraisement and refinement of zircon U–Pb isotope and trace element analyses
797 by LA-ICP-MS. Chinese Science Bulletin, 55, 1535-1546.
798 Ludwig, K.R. (2012) User's manual for Isoplot 3.75—a geochronological toolkit for
799 Microsoft Excel. Berkeley Geochronology Center Special Publication, 5, 75.
800 Marsh, J.H., and Stockli, D.F. (2015) Zircon U–Pb and trace element zoning
801 characteristics in an anatectic granulite domain: insights from lass-icp-ms depth
802 profiling. Lithos, 239, 170-185.
803 Masuda, A., Nakamura, N., and Tanaka, T. (1973) Fine structures of mutually
804 normalized rare-earth patterns of chondrites. Geochimica et Cosmochimica Acta,
805 37(2): 239-248.

Mcdonough, W.F., and Sun, S.S. (1995) The composition of the Earth. Chemical Geology, 120, 223-253.

Migdisov, A.A., Williams-Jones, A.E., Hinsberg, V.V., and Salvi, S. (2011) An experimental study of the solubility of baddeleyite (ZrO_2) in fluoride-bearing solutions at elevated temperature. Geochimica et Cosmochimica Acta, 75, 7426-7434.

Mikhailova, J.A., Pakhomovsky, Y.A., Ivanyuk, G.Y., Bazai, A.V., Yakovenchuk, V.N., Elizarova, I.R., and Kalashnikov, A.O. (2017) REE mineralogy and geochemistry of the Western Keivy peralkaline granite massif, Kola Peninsula, Russia. Ore Geology Reviews, 82, 181-197.

Möller, V., and Williams-Jones, A.E. (2016) Petrogenesis of the Nechalacho Layered Suite, Canada: Magmatic Evolution of a REE–Nb-rich Nepheline Syenite Intrusion. Journal of Petrology, 57. 229-276.

Niu, H.C., Shan, Q., Luo, Y., Yang, W.B., and Yu, X.Y. (2008) Study on the crystal-rich fluid inclusions from the Baerzhe super-large rare elements and REE deposit. Acta Petrologica Sinica, 24, 2149-2154 (in Chinese with English abstract).

Petrella, L., Williams-Jones, A.E., Goutier, J., and Walsh, J. (2014) The Nature and Origin of the Rare Earth Element Mineralization in the Misery Syenitic Intrusion, Northern Quebec, Canada. Economic Geology, 109. 1643-1666.

Qiu, K.F., and Yang, L.Q. (2011) Genetic feature of monazite and its U–Th–Pb dating: critical considerations on the tectonic evolution of Sanjiang Tethys. Acta Petrologica Sinica, 27, 2721-2732 (in Chinese with English abstract).

Qiu, Z.L., Liang, D.Y., Wang, Y.F., Sun, Y.,and Li, L.F. (2014) Zircon REE, trace element characteristics and U-Pb chronology in the baerzhe alkaline granite:

implications to the petrological genesis and mineralization. Acta Petrologica Sinica, 30, 1757-1768 (in Chinese with English abstract).

Schandl, E.S., and Gorton, M.P. (2004) A textural and geochemical guide to the identification of hydrothermal monazite: Criteria for selection of samples for dating epigenetic hydrothermal ore deposits. Economic Geology, 99, 1027-1035.

Skipton, D.R., Schneider, D.A., Mcfarlane, C.R.M., St-Onge, M.R., and Jackson, S.(2016) Multi-stage zircon and monazite growth revealed by depth profiling and in situ, U-Pb geochronology: resolving the Paleoproterozoic tectonics of the Trans-Hudson Orogen on southeastern Baffin Island, Canada. Precambrian Research, 285, 272-298.

Škoda, R., and Novák, M. (2007) Y, REE, Nb, Ta, Ti-oxide (AB2O6) minerals from REL-REE euxenite-subtype pegmatites of the Třebíč Pluton, Czech Republic; substitutions and fractionation trends. Lithos, 95(1), 43-57.

Smirnov, S.Z., Thomas, V.G., Peretyazhko, I.S., Zagorsky, V.Y., Kamenetsky, V.S., and Large, R.R., (2006) Hydrosilicate liquids in late-magmatic mineralization: experimental results and natural evidence. Geochimica et Cosmochimica Acta, 70, A598-A598.

Smirnov, S.Z., Kozmenko, O.A., and Large, R.R. (2012) Hydrosilicate liquids in the system Na_2O-SiO_2-H_2O with NaF, NaCl and Ta: evaluation of their role in ore and mineral formation at high and. Petrology, 20, 271-285.

Smirnov, S.Z., Thomas, V.G., Kamenetsky, V.S., and Kozmenko, O.A. (2017) Hydrosilicate liquids in the system rare-metal granite–Na_2O–SiO_2–H_2O as accumulators of ore components at high pressure and temperature. Petrology, 25, 625-635.

Spencer, C.J., Kirkland, C.L., and Taylor, R.J.M. (2016) Strategies towards statistically robust interpretations of in situ, U–Pb zircon geochronology. Geoscience Frontiers, 7, 581-589.

Sun, Y., Lai, Y., Chen, J., Shu, Q.H., and Yan, C. (2013) Rare earth and rare metal elements mobility and mineralization during magmatic and fluid evolution in alkaline granite system: Evidence from fluid and melt inclusions in Baerzhe granite, China. Resource Geology, 63, 239-261.

Taylor, R.D., Goldfarb, R.J., Monecke, T., Fletcher, I.R., Cosca, M.A., and Kelly, N.M. (2015) Application of U-Th-Pb phosphate geochronology to young orogenic gold deposits: new age constraints on the formation of the Grass Valley gold district, Sierra Nevada Foothills province, California. Economic Geology, 110, 1313-1337.

Tepper, J.H., and Kuehner, S.M. (1999) Complex zoning in apatite from the Idaho batholith: a record of magma mixing and intracrystalline trace element diffusion. American Mineralogist, 84, 581-595.

Thomas, R., and Davidson, P. (2016) Revisiting complete miscibility between silicate melts and hydrous fluids, and the extreme enrichment of some elements in the supercritical state—consequences for the formation of pegmatites and ore deposits. Ore Geology Reviews, 72, 1088-1101.

Valley, J.W., Kinny, P.D., Schulze, D.J., and Spicuzza, M.J. (1998) Zircon megacrysts from kimberlite: oxygen isotope variability among mantle melts. American Mineralogist, 133, 1-11.

Verplanck, P.L., and Hitzman, M.W. (2016) Introduction: Rare Earth and Critical Elements in Ore Deposits. Rev. Economic Geology, 18, 1-3.

Vielreicher, N.M., Groves, D.I., Fletcher, I.R., McNaughton, N.J., and Rasmussen, B.(2003) Hydrothermal monazite and xenotime geochronology: a new direction for precise dating of orogenic gold mineralization. SEG Newsletter, 531, 10-16

Wall, F., and Mariano, A.N. (1996) Rare earth minerals in carbonatites: a discussion centered on the Kangankunde carbonatite, Malawi. In Jones A.P., Wall F. and Williams C.T. Eds., Rare Earths Minerals: Chemistry, origin and ore deposits. Chapman and Hall, London.

Wang, Y.X., and Zhao, Z.H. (1997) Geochemistry and origin of the Baerzhe REE-Nb-Be-Zr superlarge deposit. Geochimica, 26, 24-35 (in Chinese with English abstract).

Weng, Z.H., Jowitt, S.M., Mudd, G.M., and Haque, N. (2015) A detailed assessment of global rare earth element resources: opportunities and challenges. Economic Geology, 110, 1925-1952.

Whitney, D.L., and Evans, B.W. (2010) Abbreviations for names of rock-forming minerals. American Mineralogist, 95, 185-187.

Williams, M.L., Jercinovic, M.J., and Hetherington, C.J. (2007) Microprobe Monazite Geochronology: Understanding Geologic Processes by Integrating Composition and Chronology. Annual Review of Earth and Planetary Sciences, 35, 137-175.

Williams, M.L., Jercinovic, M.J., Harlov, D.E., Budzyn, B., and Hetherington, C.J, (2011) Resetting monazite ages during fluid-related alteration. Chemical Geology, 283, 218-225.

Wu, B., Wang, R.C., Yang, J.H., Wu, F.Y., Zhang, W.L., Gu, X.P., and Zhang, A.C. (2016) Zr and REEmineralization in sodic lujavrite from the Saima alkaline complex, northeastern China: a mineralogical study and comparison with potassic rocks. Lithos, 262, 232-246.

902 Wu, C.Y., Yuan, Z.X., and Bai, G. (1996) Rare earth deposits in China. In Jones A.P.,
903 Wall F. and Williams C.T. Eds., Rare Earths Minerals: Chemistry, origin and ore
904 deposits. Chapman and Hall, London.
905 Wu, M.Q., Tian, B.F., Zhang, D.H., Xu, G.Z., Xu, W.X., and Qiu, K.F. (2018) Zircon
906 of the No. 782 deposit from the Great Xing'an Range in NE China: Implications for
907 Nb-REE-Zr mineralization during magmatic-hydrothermal evolution. Ore Geology
908 Reviews, 102, 284-299.
909 Xie, Y.L, Hou, Z.Q, Goldfarb, R.J., Guo, X., and Wang, L. (2016) Rare earth element
910 deposits in China. Rev. Economic Geology, 18, 115-136.
911 Yang, W.B. (2012) Magmatic-hydrothermal evolution of alkaline granite and it
912 constraints on the rare-metal mineralization: A case study of the Baerzhe
913 REE-Nb-Be-Zr deposit, 160 p. PhD. Thesis, University of Chinese Academy of
914 Sciences, Beijing (in Chinese with English abstract).
915 Yang, W.B., Niu, H.C., Shan, Q., Luo, Y., and Yu, X.Y. (2009) Ore-forming mechanism
916 of the Baerzhe super-large rare and rare earth elements deposit. Acta Petrologica
917 Sinica, 25, 2924-2932 (in Chinese with English abstract).
918 Yang, W.B., Su, W.C., Liao, S.P., Niu, H.C., Luo, Y., Shan, Q., and Li, N.B. (2011)
919 Melt and melt-fluid inclusions in the Baerzhe alkaline granite: Information of the
920 magmatic-hydrothermal transition. Acta Petrologica Sinica, 27, 1493-1499 (in
921 Chinese with English abstract).
922 Yang, W.B., Niu, H.C., Sun, W.D., Shan, Q., Zheng, Y.F., Li, N.B., Li, C.Y., Arndt,
923 N.T., Xu, X., Jiang, Y.H., and Yu, X.Y. (2013) Isotopic evidence for continental ice
924 sheet in mid-latitude region in the supergreenhouse Early Cretaceous. Scientific
925 Reports, 3, 2732.

Yang, W.B., Niu, H.C., Shan, Q., Sun, W.D., Zhang, H., Li, N.B., Jiang,Y.H., and Yu, X.Y.(2014) Geochemistry of magmatic and hydrothermal zircon from the highly evolved Baerzhe alkaline granite: implications for Zr–REE–Nb mineralization. Mineralium Deposita, 49, 451-470.

Yuan, Z.X., Bai, G., and Ding, X.S. (1980) Mineralogy and geochemistry of the "801" alkaline porphyric rare metal deposit. Institute of Geology Chinese Academy of Geological Sciences: Research Report, 30, 1-108 (in Chinese with English abstract).

Yuan, Z.X., Zhang, M., and Wan, D.F. (2003) A discussion on the petrogenesis of 18O-low alkali granite—a case study of Baerzhe alkali granite in Inner Mongolia. Acta Petrol. Miner., 22, 119-124 (in Chinese with English abstract).

Yuan, Z.X., Bai, G., Yang, Z.Q., and Yang, Y.Q. (2007) The self-metasomatism of ore in rare metal and rare earth deposits and it implication. In Yu X.G. Eds., Festschrift of Academician Guo Chengji. Guangdong Science and Technology Press, Guangdong (in Chinese with English abstract).

Zhang, M., and Yuan, Z.X. (1988) Isotope geochemistry of "801" rare mental alkali granite in inner Mongolia. Geological Institute of the Chinese Academy of Geological Sciences Collection, 1, 139-146 (in Chinese with English abstract).

Zhao, Z.H., Xiong, X.L., Hen, X.D., Wang, Y.X., Qiang, W., Bao, Z.W., and Jahn, B. (2002) Controls on the REE tetrad effect in granites: evidence from the Qianlishan and Baerzhe granites, China. Geochemical Journal, 36, 527-543.

Zhu, X.K., O'Nions, R.K., Belshaw, N.S., and Gibb, A.J. (1997) Significance of in situ SIMS chronometry of zoned monazite from the Lewisian granulites, northwest Scotland. Chemical Geology, 135, 35-53.

949 Zhu, X.K., and O'Nions, R.K. (1999) Monazite chemical composition: Some
950 implications for monazite geochronology. Contributions to Mineralogy and
951 Petrology, 137, 351-363.

952 **Figures Captions**

953 Figure 1. (a) GoogleEarth image showing the location of the Baerzhe REE-Nb-Zr-Be
954 deposit (Inner Mongolia, China). (b) Sketch geological map of the Baerzhe deposit
955 showing the phase relationship of the Baerzhe alkaline igneous complex. (c) Simplified
956 cross section geological profile labeled in Figure 1b by Line A-A' showing the five
957 lithologic facies and their relationship to Late Jurassic volcanic rocks recognized by
958 mapping from the drilling hole samples (modified after Yuan et al. 1980; Jahn 2004; Niu
959 et al. 2008; Sun et al. 2013).

960

961 Figure 2. Hand specimen of the representative samples studied in this work showing the
962 texture and mineral assemblage.

963

964 Figure 3. Photomicrographs showing texture and mode of occurrence of Type Ia zircons
965 (a: cross-polarized transmitted light. b, d: CL image. c: plane-polarized transmitted light).

966

967 Figure 4. Photomicrographs showing texture and mode of occurrence of Type Ib zircons
968 (a: plane-polarized transmitted light. b, c, e, f: CL image. d: cross-polarized transmitted
969 light).

970

971 Figure 5. Photomicrographs showing texture and mode of occurrence of Type II zircons
972 (a, c: plane-polarized transmitted light. b, f: CL image. d, e: BSE image).

973

974 Figure 6. Photomicrographs showing texture and mode of occurrence of monazite grains
975 (a: plane-polarized transmitted light. b, c: cross-polarized transmitted light. d, e, f: BSE
976 image). Note the numbers 1 and 2 in figure d and numbers 28 and 29 in figure e are the
977 number of EPMA spot.

978

979 Figure 7. The REE distribution patterns of Type Ia (a), Type Ib (b), and Type II(c)
980 zircons analyzed by LA-ICP-MS, and that of monazite grains (d) determined by EPMA.
981 Elemental values below the electron microprobe detection limits are not shown. Bulk
982 rock REE concentrations of mineralization and barren granites from Yang (2012) are
983 plotted for comparison. The REE concentrations are normalized to the chondrite
984 composition reported by McDonough and Sun, 1995.

985

986 Figure 8. In situ LA-ICP-MS U-Pb Tera–Wasserburg Concordia diagrams of Type Ia (a),
987 Type Ib (b), and Type II (c) zircon, and monazite grains (d). The ^{207}Pb-corrected
988 ^{206}Pb/^{238}U ages are present and plotted because the analyzed data yield low U abundances
989 and elevated common Pb contents resulting from possible matrix effects and subsequent
990 hydrothermal fluids overprinting.

991

Figure 9. Geological time frame of the Zr and REE mineralization of the Baerzhe REE-Nb-Zr-Be deposit and its genetically related alkaline igneous complex constrained by crosscutting relationships and geochronology. Compiled geochronological data are provided in Table 1, and are from Zhang and Yuan (1988), Wang and Zhao (1997), Yuan et al. (2003), Yang (2012), Qiu et al. (2014), Yang et al. (2014) and this study.

Tables Captions

Table 1 Geochronological data compilation of the Baerzhe deposit.

Table 2 Comparison between zircon with monazite

Supplementary Tables

Supplementary Table 1 In situ LA-ICP-MS trace element data (ppm) of zircon grains.

Supplementary Table 2 In situ electron microprobe geochemical data (in weight percent) of monazite grains.

Supplementary Table 3 In situ LA-ICP-MS U-Pb data of zircon grains.

Supplementary Table 4 In situ LA-ICP-MS U-Pb data of monazite grains.

1013

1014

1013 # Tables

1014 Table 1 Geochronological data compilation of the Baerzhe deposit.

No.	Sample	Age (Ma)	Mineral	Method	Analyses number	Reference
1	Baerzhe alkaline granite	127.2±5.5	Whole rock	Rb-Sr isochron	6	Zhang and Yuan, 1988
2	Baerzhe albite granite	125.2±2	Whole rock	Rb-Sr isochron	6	Wang and Zhao, 1997
3	Alkaline granite	127.2	Whole rock	Rb-Sr isochron	Not available	Yuan et al., 2003
4	Alkaline granite	121.6±2.3	Whole rock	Rb-Sr isochron	15	Yang, 2012
5	Alkaline granite	123.1±2.3	Zircon	LA-ICP-MS	14	Yang, 2012
6	Baerzhe alkaline granite	122.7±1.8	Light and dark colored zircon	LA-ICP-MS	34	Qiu et al., 2014
7	Alkaline granite	123.9±1.2	Magmatic zircon	SIMS	17	Yang et al., 2013
8	Alkaline granite	123.5±3.2	Hydrothermal zircon	SIMS	7	Yang et al., 2013
9	Alkaline granite	127.2 ± 1.3	Least altered magmatic zircon	LA-ICP-MS	13	This study
10	Alkaline granite	125.40 ± 0.73	Strongly altered magmatic zircon	LA-ICP-MS	28	This study
11	Alkaline granite	124.86 ± 0.63	Deuteric zircon	LA-ICP-MS	29	This study
12	Alkaline granite	122.82 ± 0.62	Hydrothermal zircon	LA-ICP-MS	37	This study

1015

This is a preprint, the final version is subject to change, of the American Mineralogist (MSA)
Cite as Authors (Year) Title. American Mineralogist, in press.
DOI: https://doi.org/10.2138/am-2019-6890

1016 Table 2 Comparison between zircon with monazite

Features	Zircon			monazite
	Type Ia	Type Ib	Type II	
Color	light green; transparent	pale brown; translucent	murky-brown; translucent	colorless; transparent
Occurrence	individual crystal	individual crystal or aggregates	aggregates	individual crystal or aggregates
Texture	euhedral	euhedral, subhedral	subhedral, anhedral and core-mantle	euhedral to anhedral; fluid mediated coupled dissolution–precipitation
Mineral association	quartz, perthite, albite, sodic amphibole	quartz, perthite, albite, sodic amphibole		Euxenite, bastnäsite, hingganite, synchysite
Growth zone	well-developed and bright oscillatory growth zoning	well-developed and dark oscillatory growth zoning	inner part like weaving guts, and well-developed and dark oscillatory zonation at the rim	no zonation by CL and BSE imaging
Geochemistry	flat and low LREE; strongly enriched HREE; distinct negative Eu anomalies	enriched and negative slope patterns in LREE, moderate enriched and positive slope in HREE pattern	flat and low REE; distinct negative Eu anomalies	enriched in LREE; relative depletion in HREE; distinct positive Eu anomalies
Origin	magmatic and least-altered by deuteric fluid	magmatic and strongly altered by deuteric fluid	late magmatic/ deuteric fluid	hydrothermal
Age (Ma)	127.2 ± 1.3	125.4 ± 0.7	124.9± 0.6	122.8 ± 0.6

1017

1018

This is a preprint, the final version is subject to change, of the American Mineralogist (MSA)
Cite as Authors (Year) Title. American Mineralogist, in press.
DOI: https://doi.org/10.2138/am-2019-6890

Figure 1.

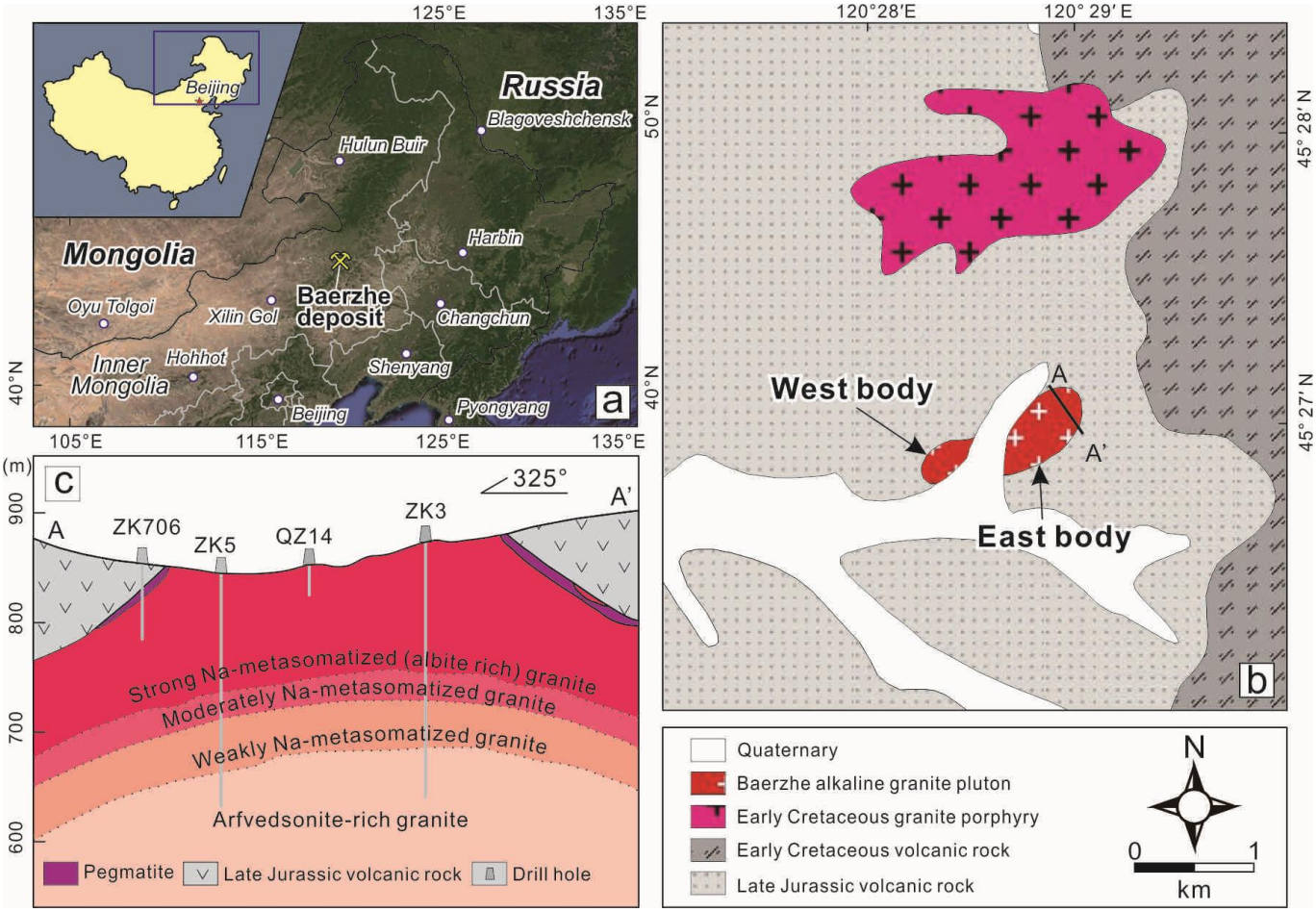

This is a preprint, the final version is subject to change, of the American Mineralogist (MSA)
Cite as Authors (Year) Title. American Mineralogist, in press.
DOI: https://doi.org/10.2138/am-2019-6890

Figure 2.

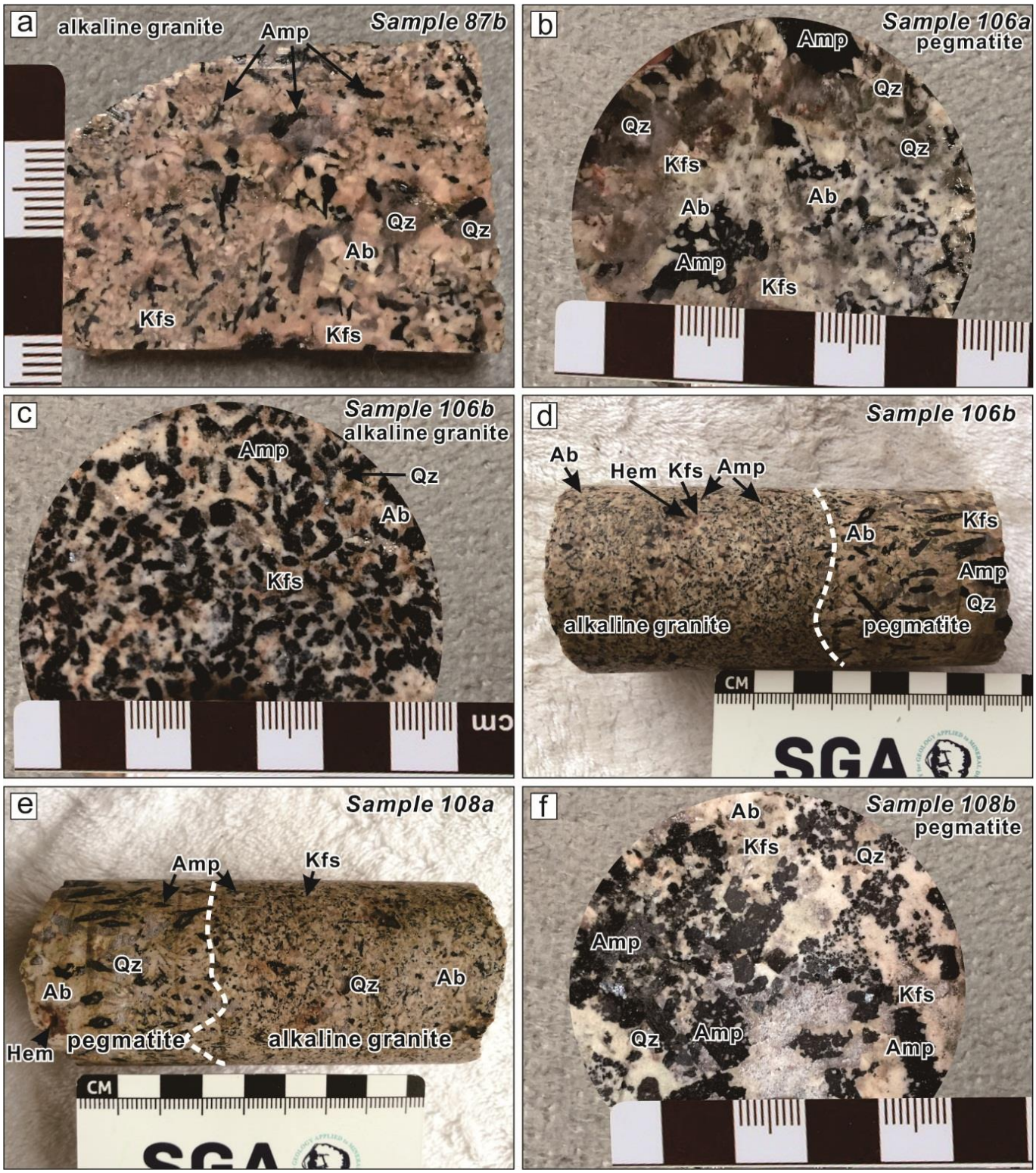

This is a preprint, the final version is subject to change, of the American Mineralogist (MSA)
Cite as Authors (Year) Title. American Mineralogist, in press.
DOI: https://doi.org/10.2138/am-2019-6890

Figure 3.

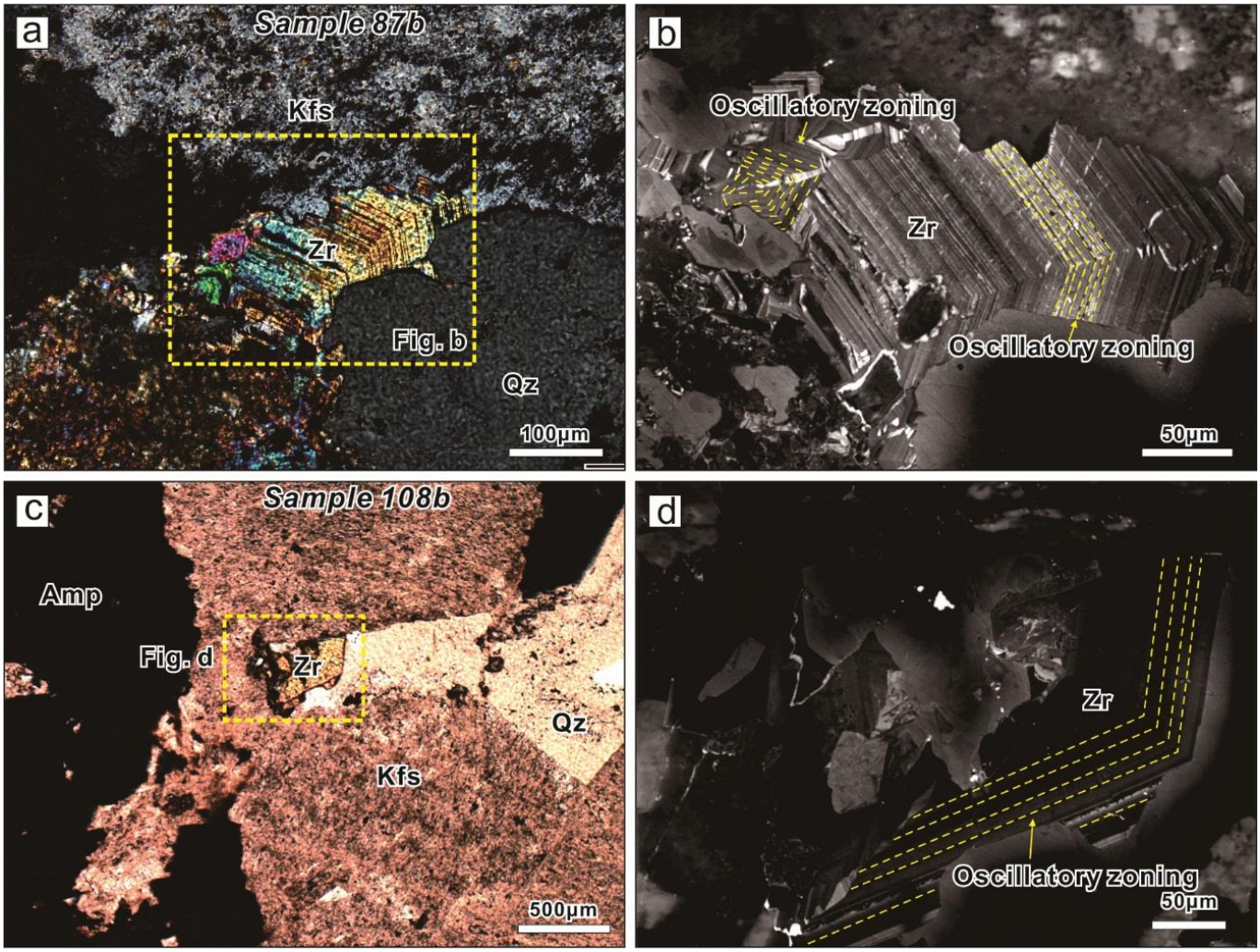

This is a preprint, the final version is subject to change, of the American Mineralogist (MSA)
Cite as Authors (Year) Title. American Mineralogist, in press.
DOI: https://doi.org/10.2138/am-2019-6890

Figure 4.

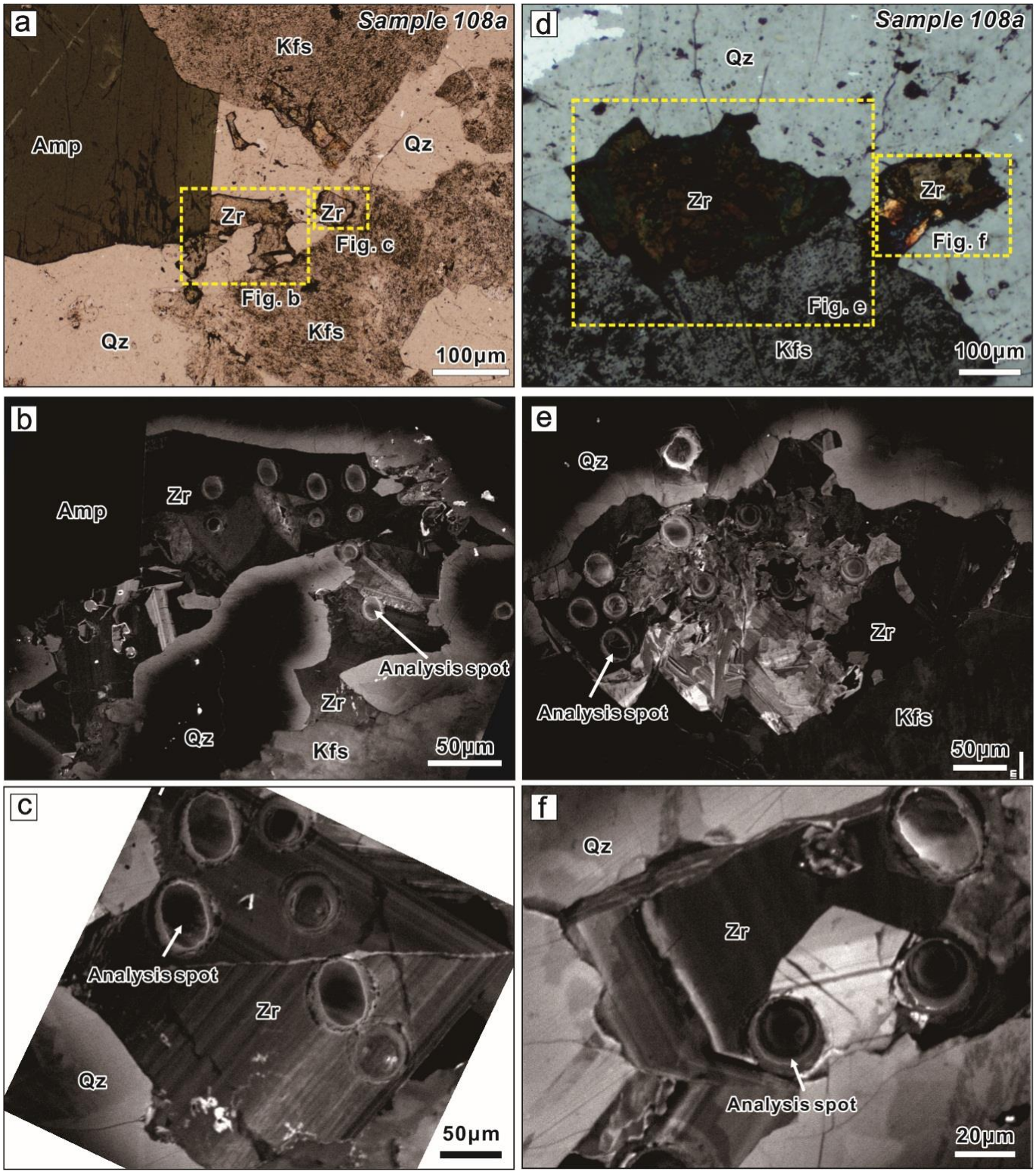

This is a preprint, the final version is subject to change, of the American Mineralogist (MSA)
Cite as Authors (Year) Title. American Mineralogist, in press.
DOI: https://doi.org/10.2138/am-2019-6890

Figure 5.

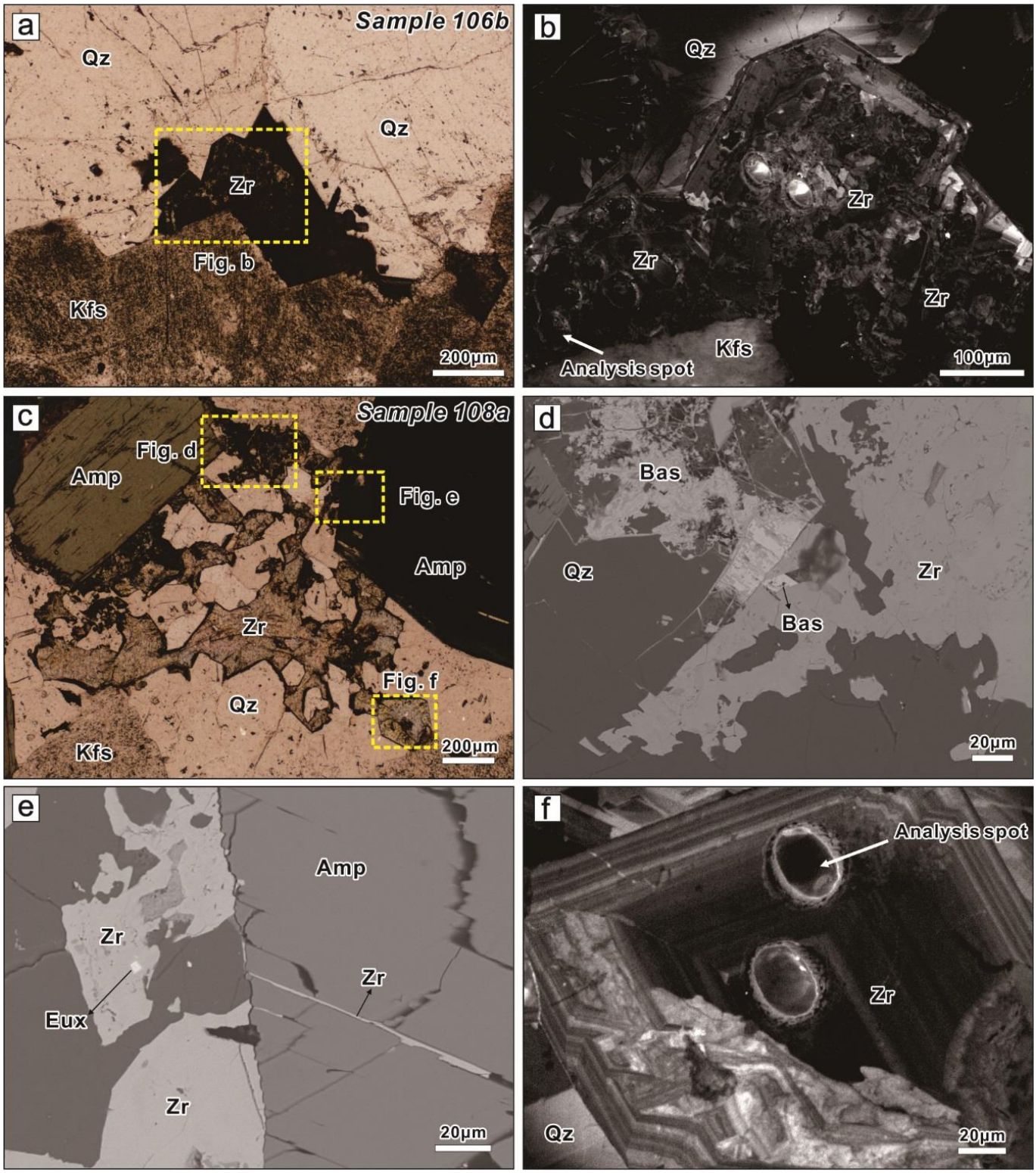

This is a preprint, the final version is subject to change, of the American Mineralogist (MSA)
Cite as Authors (Year) Title. American Mineralogist, in press.
DOI: https://doi.org/10.2138/am-2019-6890

Figure 6.

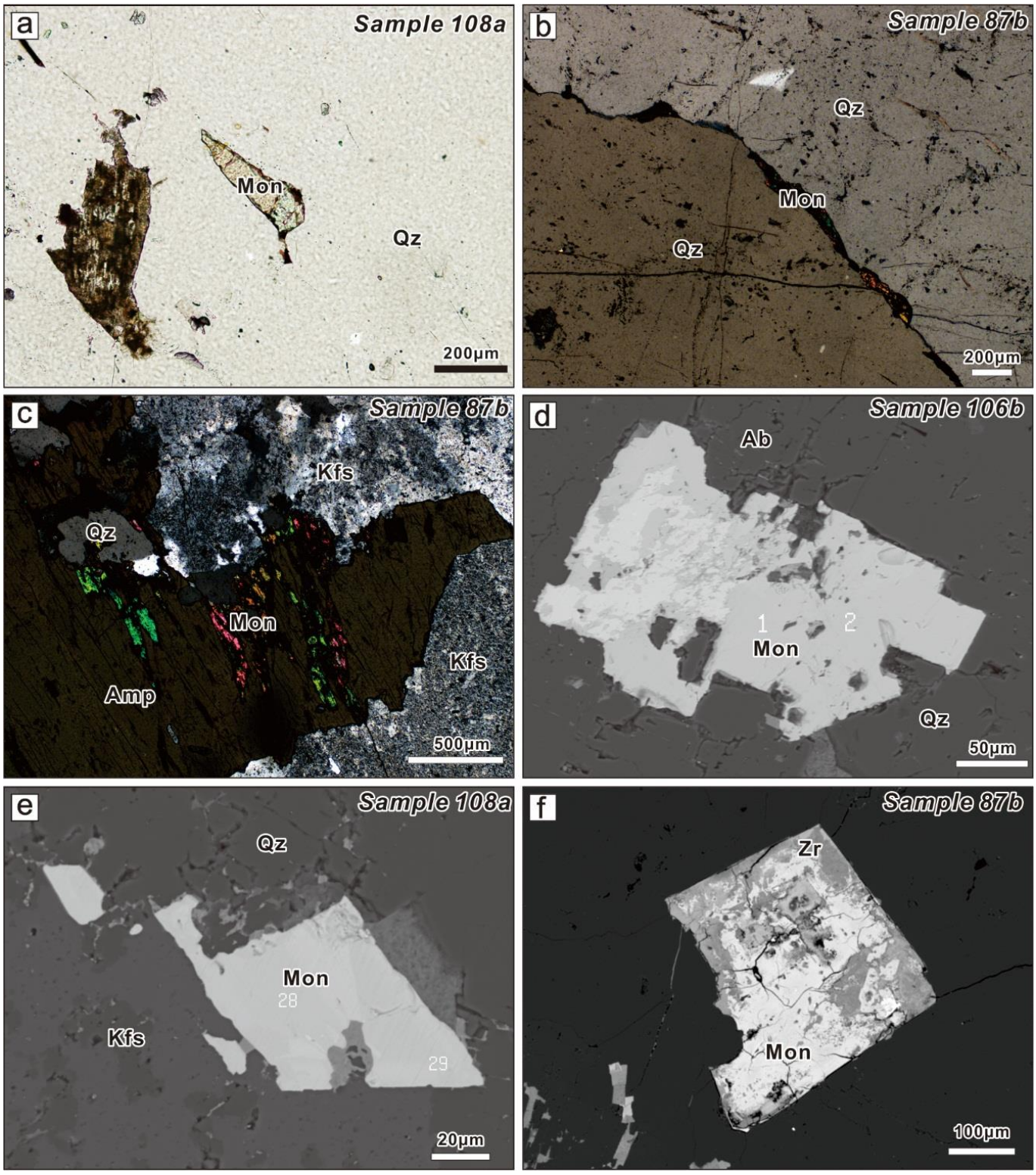

This is a preprint, the final version is subject to change, of the American Mineralogist (MSA)
Cite as Authors (Year) Title. American Mineralogist, in press.
DOI: https://doi.org/10.2138/am-2019-6890

Figure 7.

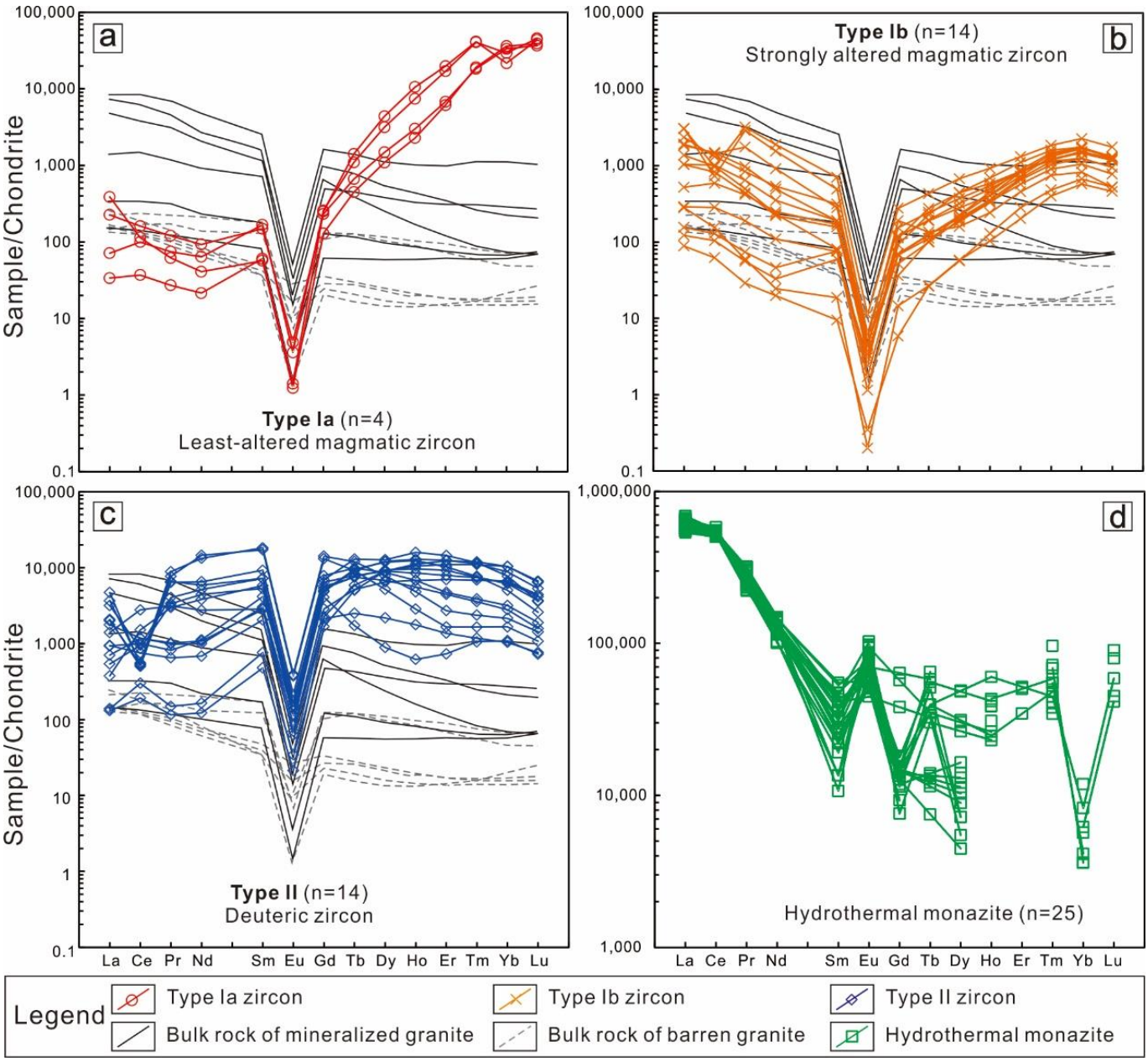

This is a preprint, the final version is subject to change, of the American Mineralogist (MSA)
Cite as Authors (Year) Title. American Mineralogist, in press.
DOI: https://doi.org/10.2138/am-2019-6890

Figure 8.

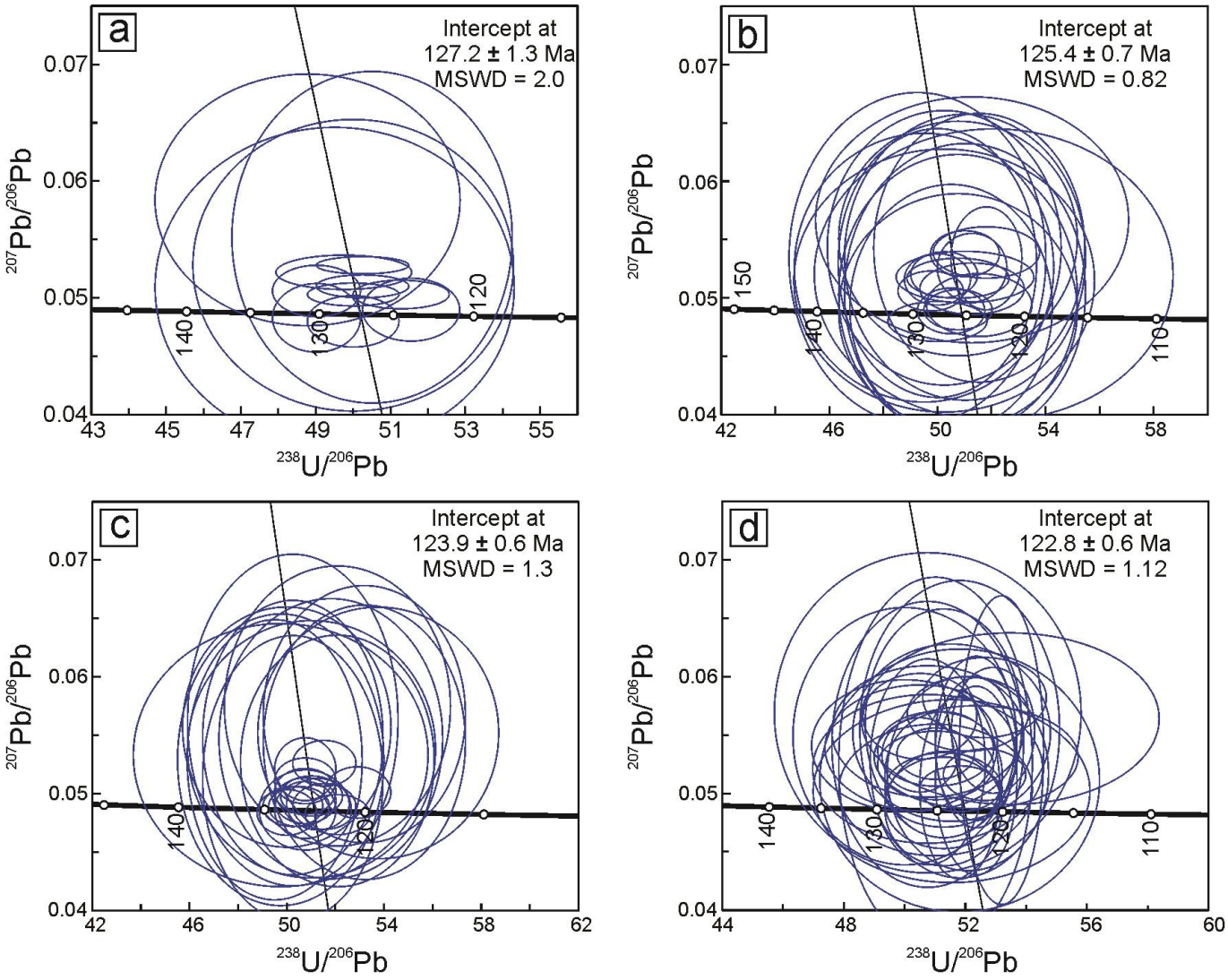

This is a preprint, the final version is subject to change, of the American Mineralogist (MSA)
Cite as Authors (Year) Title. American Mineralogist, in press.
DOI: https://doi.org/10.2138/am-2019-6890

Figure 9.